Singular Fluctuational Electrodynamic Effects in Hyperbolic Metamaterials and Moving Media

by

Yu Guo

A thesis submitted in partial fulfillment of the requirements for the degree of

Master of Science
in
Photonics and Plasmas

Department of Electrical and Computer Engineering
University of Alberta

Abstract

Metamaterials are artificial media designed to achieve exotic electromagnetic responses that are not available in conventional materials. Engineering the black body thermal emission using metamaterials promises to impact a variety of applications involving thermophotovoltaics, energy management and coherent thermal sources. Metamaterials with hyperbolic dispersion exhibit a broadband singularity in the bulk photonic density of states, which can be thermally excited and utilized in various thermal applications.

In this report, we give a detailed account of equilibrium and non-equilibrium fluctuational electrodynamics of hyperbolic metamaterials. We show the unifying aspects of two different approaches; one utilizes the second kind of fluctuation dissipation theorem and the other makes use of the scattering method. We show the existence of broadband thermal emission and heat transfer beyond the black body limit in the near field. This arises due to the thermal excitation of unique bulk metamaterial modes, which do not occur in conventional media. We analyze the near-field of hyperbolic metamaterials at finite temperatures and show that the lack of spatial coherence can be attributed to the multi-modal nature of super-Planckian thermal emission. We also adopt the analysis to phonon-polaritonic super-lattice metamaterials and describe the regimes suitable for experimental verification of our predicted effects. The results also reveal that far-field thermal emission spectra are dominated by epsilon-near-zero and epsilon-near-pole responses as expected from Kirchoff's

laws. Our work should aid both theorists and experimentalists to study complex media and engineer equilibrium and non-equilibrium fluctuations for applications in thermal photonics.

In the second part, we describe our discovery of a singular resonance with infinite quality factor which occurs between moving plates. Conventional resonators fold the path of light by reflections leading to a phase balance and thus constructive addition of propagating waves. However, amplitude decrease of these waves due to incomplete reflection or material absorption leads to a finite quality factor of all resonances. Here we report on our result that evanescent waves can lead to both a phase and amplitude balance causing an ideal and Fabry-Perot resonance condition in spite of material absorption and non-ideal boundary discontinuities. The counterintuitive resonance occurs if and only if the Fabry-Perot plates are in relative motion to each other separated by a critical distance. We show that this singular resonance can be thermally excited between moving plates separated by a small gap causing a large number of photons to be exchanged between them. Furthermore, we also show that this resonance fundamentally dominates all non-equilibrium interactions (momentum and heat transfer) between the moving bodies. Our result is valid in the relativistic limit considering polarization mixing and also reveals the important role of the singular resonance on the fluctuational drag force between moving bodies in the $T \rightarrow 0$ limit (quantum friction).

Preface

Chapter 2 and part of Chapter 1 of this thesis have been published in Yu Guo, Zubin Jacob, "Fluctuational electrodynamics of hyperbolic metamaterials," J. Appl. Phys. 115, 234306 (2014) and Yu Guo, Zubin Jacob, "Thermal hyperbolic metamaterials," Optics Express 21 (12), 15014-15019 (2013). I was responsible for developing the theory, analyzing the results and writing the manuscript. Zubin Jacob assisted with the theory development and contributed to manuscript edits. Zubin Jacob was the supervisory author and was involved with concept formation, analysis and manuscript writing.

Another part of Chapter 1 of this thesis has been published in a review paper as Yu Guo, Ward Newman, Cristian L. Cortes, and Zubin Jacob, "Applications of Hyperbolic Metamaterial Substrates," Advances in OptoElectronics Volume 2012 (2012). Yu Guo, Ward Newman and Cristian L. Cortes, three graduate students supervised by Zubin Jacob, prepared the figures and conducted research on the topics reviewed. Zubin Jacob wrote the manuscript.

Chapter 3 and Appendix A of this thesis have been posted on the arXiv, as Yu Guo and Zubin Jacob, "Singular evanescent wave resonance," arXiv:1311.3718 [physics.optics]. Zubin Jacob introduced the topic to me, I learned the theory and found the key result. We both contributed to physical interpretations of the results and manuscript preparation.

I would like dedicate this work to my mother, Huiping Lü, my father, Gewen Guo, and my younger sister, Qi Guo, for their endless love and support

Acknowledgements

Foremost, I would like to express my deepest gratitude to my advisor Professor Zubin Jacob. Three years ago, when I was an undergraduate intern in Zubin's group, it was Zubin who taught me to start from solving simple, basic but fundamental problems and gave me the first sense of real scientific research. During the two years of graduate life, Zubin has always been ready for help whenever I had questions or troubles in research. Zubin has patiently and encouragingly taught me to work passionately, think intuitively, explain clearly and write precisely. I also greatly appreciate the freedom he offered in choosing research projects when we came up with several worth-trying ideas.

Great thanks to the group members: Sean Molesky, Ward Newman, Cris Cortes, Prashant Shekhar, Jon Atkinson, Saman Jahani, Huan Hu and Farid Kalhor, for your help, knowledge, discussions, suggestions, and most importantly, friendship. Thank you all for making my time at University of Alberta a wonderful experience.

Last but not least, I would like to thank my family, my parents Huiping Lü and Gewen Guo and my younger sister Qi Guo for all your encouragement and support. I might be somewhat selfish to pursue graduate study abroad, but you always stand by my decision. I will not let you down.

Contents

List of Figures

List of Abbreviations

Abbreviation	Extended Form
HMM	Hyperbolic Metamaterial
FDT	Fluctuation Dissipation Theorem
DGF	Dyadic Green's Function
EMT	Effective Medium Theory
TMM	Transfer Matrix Method
ENZ	Epsilon-Near-Zero
ENP	Epsilon-Near-Pole
LDOS	Local Density of States
SPP	Surface Plasmon Polariton
SPhP	Surface Phonon Polariton
SWR	Surface Wave Resonance
FP	Fabry-Perot
Re	Real Component of Expression
Im	Imaginary Component of Expression
Tr	Trace of matrix

Chapter 1

Introduction

The foundations of analyzing thermal and vacuum fluctuations of the electromagnetic field inside matter were laid in the seminal work of S. M. Rytov [1]. Every point in space is associated with electromagnetic fluctuations (currents), which obey specified second order correlations, through the framework of fluctuation dissipation theorem (FDT) [1,2]. The magnitude of these fluctuations depends on the temperature and the macroscopic conductivity of the media. Conventionally, the FDT that specifies correlation of the random currents is called the second kind of FDT [1,3]. In global thermal equilibrium, FDT can also specify the correlation of electromagnetic fields directly, which is called the first kind of FDT [1,3]. Provided the information of the sources, Dyadic Green's function (DGF) [4,5], which is the electromagnetic propagator relating point sources to electromagnetic fields, can completely specify the electromagnetic fields. Theoretically, combining FDT and DGF, we are able to calculate the energy density, Poynting vector, spatial coherence of the electromagnetic fields for any physical structure, if the optical constants and temperatures are known.

Rytov's work gave rise to a unified approach of understanding fluctuational forces [6] (Lifshitz theory of Casimir forces), near field thermal emission and radiative heat transfer [7–30]. (Polder-Van-Hove theory [7]). Recent developments in nanoengineering and detection have led to experimental regimes [28–34] where these effects can play a dominant role. Simultaneously, theoretical work has shed light on the fact that the classical scattering matrix along with the temperatures of objects of various geometries can completely

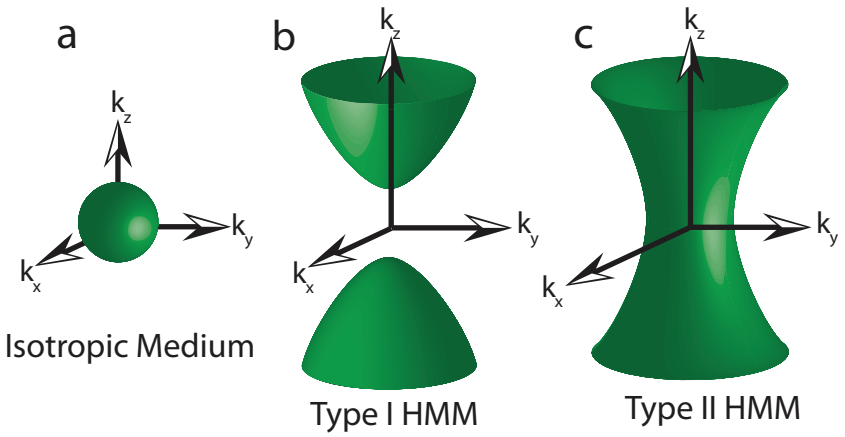

Figure 1.1: (a) The isofrequency contour for an isotropic dielectric is a sphere. For extraordinary waves in an extremely anisotropic uniaxial medium, the isofrequency contour becomes a hyperboloid which supports waves with unbounded wavevectors, in stark contrast to an isotropic medium. (b) A type I HMM has one component of the dielectric tensor negative ($\epsilon_{xx} = \epsilon_{yy} > 0$ and $\epsilon_{zz} < 0$) and supports low-k and high-k waves. (c) A type II HMM has two components of the dielectric tensor negative ($\epsilon_{xx} = \epsilon_{yy} < 0$ and $\epsilon_{zz} > 0$) and only supports high-k waves.

characterize these fluctuations in both equilibrium and non-equilibrium situations [35–47].

Metamaterials (artificial photonic media) are emerging as a novel concept to engineer the scattering matrix and achieve exotic electromagnetic responses which are beyond those available in conventional materials [48–50]. A large body of work has emerged in the last decade which in principle engineers the classical scattering matrix to achieve effects such as negative refraction [51, 52], enhanced chirality [51–55], invisibility [56–58] and subwavelength imaging [56–60]. Recently, it was shown that a specific class of metamaterials, known as hyperbolic metamaterials [60–66](indefinite media) has the potential for thermal engineering. Such media support unique modes which can be thermally excited and detected in the near-field due to the super-Planckian nature of their thermal emission spectrum [12, 67–71].

Hyperbolic metamaterials (HMMs) can be considered as uniaxial metacrystals with an extremely anisotropic dielectric tensor [62], $\overleftrightarrow{\epsilon} = diag[\epsilon_{xx}, \epsilon_{yy}, \epsilon_{zz}]$ such that $\epsilon_{xx} = \epsilon_{yy}$ and $\epsilon_{xx}\epsilon_{zz} < 0$. The properties of HMMs are best understood by studying the isofrequency surface of extraordinary waves in this

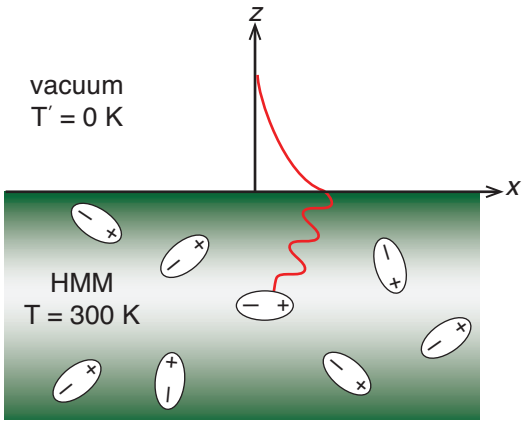

Figure 1.2: Propagating waves with large wavevector inside HMMs could tunnel out to become evanescent waves in the near field, leading to broadband super-Planckian thermal emission.

medium

$$\frac{k_x^2 + k_y^2}{\epsilon_{zz}} + \frac{k_{zp}^2}{\epsilon_{xx}} = \frac{\omega^2}{c^2} \tag{1.1}$$

The above equation represents a hyperboloid when $\epsilon_{xx}\epsilon_{zz} < 0$ which is an open surface in stark contrast to the closed spherical dispersion in an isotropic medium (Fig. 1.1). The immediate physical consequence of this dispersion relation is the existence of propagating waves with large wavevectors known as high-k waves which are evanescent in conventional media. Furthermore, the density of states, which is proportional to the volume between two adjacent iso-frequency contours, can be infinite inside HMMs in the ideal case (when no optical losses are considered). The singularity in the bulk photonic density of states [72] is directly related to the removal of the upper cutoff of wavevectors on the iso-frequency surface. For thermal applications, we show that the high wavevector states tunnel out from HMMs and contribute to the thermal energy transport (Fig. 1.2). Since these wavevectors are much larger than the free space wavevector, this enhancement of thermal energy can only occur in the near field. Besides, the extreme anisotropic dielectric tensor doesn't rely on resonant effects and can be achieved over a broad frequency region. Using this idea, the near field emissivity of hyperbolic metamaterials can be largely enhanced over broad frequency regions [12], in contrast to mechanisms based on resonant effects (for example, surface waves), where enhancement occurs only in a narrow band [11].

We now introduce nomenclature to classify the two types of hyperbolic

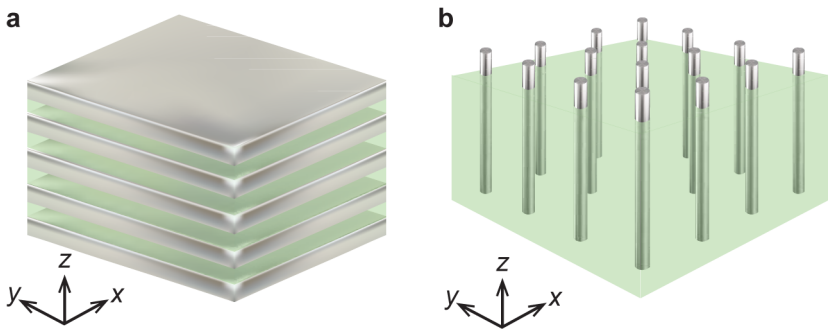

Figure 1.3: (a) Multilayer realization of hyperbolic metamaterials consisting of alternating subwavelength layers of metal and dielectric (b) metal nanorod array in a dielectric host matrix.

metamaterials based on the number of components of the dielectric tensor which are negative [61]. Note that if all three components are negative, we have an effective metal and propagating waves are not allowed in such a medium. Type I: If there is only one component negative i.e. $\epsilon_{zz} < 0$ in the tensor, then we term such metamaterials as type I HMM. They have low loss because of their predominantly dielectric nature but are difficult to achieve in practice. Type II: If there are two components in the dielectric tensor which are negative i.e. $\epsilon_{xx} = \epsilon_{yy} < 0$, we term them as type II HMMs. They have higher loss and high impedance mismatch with vacuum due to their predominantly metallic nature.

There are two prominent methods to engineer practical hyperbolic media. The first consists of alternating layers of metal and dielectric with the layer thicknesses far below the size of the wavelength. The second approach consists of metal nanorods in a dielectric host such as porous anodic alumina (AAO). Figure 1.3 is a schematic illustration of these two approaches. Both these approaches achieve the desired extremely anisotropic response according to Maxwell-Garnett effective medium theory [73–77]. It is important to note that effective medium theory predicts the desired response in a broad spectral bandwidth because of its non-resonant nature. This is crucial since absorption in resonant metamaterials are a major detriment to practical applications.

In chapter 2, we adopt the techniques of fluctuational electrodynamics to provide a first-principle account of the thermal emission characteristics of hyperbolic metamaterials. We show that the conventional approach of utilizing the second kind of fluctuation dissipation theorem [1,3,78] is equivalent to the scattering matrix method [3,35,43,78] for calculating the metamaterial energy

density. We specifically provide the derivations of the fluctuational effects in both effective medium theory and practical thin film multilayer metamaterial designs [61, 79]. While the characteristics can in principle be obtained from formulas related to the reflection coefficients, it does not shed light on various aspects of equilibrium or non-equilibrium fluctuations in the context of metamaterials. Our aim is to provide an insightful look at prevailing approaches adopted to the case of hyperbolic metamaterials.

We also consider the case of a practical phonon-polaritonic metamaterial [12, 80] and show the stark contrast in the far-field and near-field thermal emission characteristics [11]. This should help experimentalists design experiments starting from analyzing the far-field characteristics, retrieving effective medium characteristics and then look for our predicted near-field effects. We show that the far-field characteristics are dominated by the epsilon-near-zero and epsilon-near-pole responses as expected from Kirchoff's laws [81]. This is true independent of material choice and can occur for both nanowire and multilayer hyperbolic metamaterials [81]. We comment here that for practical applications high temperature plasmonics and metamaterials would be needed [81].

We also study the limitations of effective medium theory (EMT) but focus on cases where there is good agreement between practical structures and EMT [61, 79, 82]. We emphasize that it is known in the metamaterials community that the unit cell of a metamaterial can show characteristics similar to the bulk medium [61]. In the context of thin film hyperbolic metamaterials, this was experimentally elucidated in Ref. [83] and theoretically explained in detail in Ref. [61].

In this work we also describe another effect connected to hyperbolic super-Planckian thermal emission [12]. We analyze the spatial coherence [13, 84–87] of the near-field thermal emission and relate it to the metamaterial modes. We show that there is a subtle interplay in near-field spatial coherence due to competition between surface waves and hyperbolic modes. We expect our work to aid experimentalists in isolating thermal effects related to metamaterials and also form the theoretical foundation for developing the macroscopic quantum electrodynamics [88] of HMMs.

In chapter 3, we present our work on momentum transfer between two moving plates, intrigued by the controversial quantum friction problem–if there exist lateral Casimir forces exist between two plates moving parallel to each

other at constant speed at zero temperature [21, 38, 89–102]. We interpret the lateral force as momentum transfer through photon exchange between the moving plates [38]. We argue that the stark difference of zero temperature Bose-Einstein occupation number at positive and negative frequency should be responsible for the existence of quantum friction.

More importantly, we report our discovery on a fundamentally new Fabry-Perot resonance of evanescent waves bouncing between two relatively moving mirrors. Unlike any other conventional resonance, the quality factor of this resonance can be infinite in spite of material absorption and dispersion. This singular resonance leads to infinitely many photons exchanged between two relatively moving mirrors even at zero temperature. We further demonstrate that fluctuational electrodynamic forces between the mirrors can be infinitely large due to the singular Fabry-Perot resonance of evanescent waves, challenging the conventional viewpoint that phenomena dealing with vacuum fluctuations are too weak to be detected. The singular resonance should be detectable in nano-electro-mechanical systems and can shed light on interaction between moving bodies at the nanoscale.

Chapter 2

Thermal emission and heat transfer

2.1 Fluctuation dissipation theorem

In global thermal equilibrium, the first kind of fluctuation dissipation theorem [1, 3](FDT) directly specifies the correlation function of electric fields. It is expressed by

$$\left\langle \vec{E}(\boldsymbol{r}_1,\omega)\otimes\vec{E}^*(\boldsymbol{r}_2,\omega')\right\rangle = \frac{\mu_0\omega}{\pi}\Theta(\omega,T)\,\mathrm{Im}\overleftrightarrow{G}(\boldsymbol{r}_1,\boldsymbol{r}_2,\omega)\delta(\omega-\omega'). \tag{2.1}$$

Here $\overleftrightarrow{G}$ is the dyadic Green's function [4,5](DGF), $\Theta(\omega,T)=\hbar\omega/(e^{\hbar\omega/k_BT}-1)$ is the mean energy of a thermal oscillator.

Eq. (2.1) has two main applications. Firstly, it can be used to derive the electromagnetic stress tensor at a certain point. Secondly, it directly gives the cross-spectral density tensor [84, 87] which characterizes the spatial coherence of a thermal radiative source. The second kind of FDT [1,3] that specifies the correlation function of thermally generated random currents is

$$\left\langle \vec{j}(\boldsymbol{r}_1,\omega)\otimes\vec{j}^*(\boldsymbol{r}_2,\omega')\right\rangle = \frac{\omega\epsilon_0}{\pi}\boldsymbol{\epsilon}''(\omega)\Theta(\omega,T)\delta(\boldsymbol{r}_1-\boldsymbol{r}_2)\delta(\omega-\omega'). \tag{2.2}$$

We assume the permittivity $\boldsymbol{\epsilon}$ is a diagonal matrix; $\boldsymbol{\epsilon}''$ denotes the imaginary part.

The first kind of FDT can only be used in global thermal equilibrium. In non-equilibrium situation, we should first employ Maxwell equations to obtain

the electromagnetic fields generated by random currents through the DGF,

$$\vec{E}(\boldsymbol{r}) = i\omega\mu_0 \iiint \overleftrightarrow{G}(\boldsymbol{r}, \boldsymbol{r}')\vec{j}(\boldsymbol{r}')d\boldsymbol{r}', \tag{2.3}$$

$$\vec{H}(\boldsymbol{r}) = \iiint \nabla \times \overleftrightarrow{G}(\boldsymbol{r}, \boldsymbol{r}')\vec{j}(\boldsymbol{r}')d\boldsymbol{r}', \tag{2.4}$$

and then calculate the electromagnetic stress tensor or the cross-spectral density tensor.

The dyadic Green's function (DGF) satisfies an important identity [3, 103],

$$\mathrm{Im}\,\overleftrightarrow{G}(\boldsymbol{r}_1, \boldsymbol{r}_2, \omega) = \frac{\omega^2}{c^2}\int_V \overleftrightarrow{G}(\boldsymbol{r}_1, \boldsymbol{r}', \omega)\boldsymbol{\epsilon}''(\boldsymbol{r}', \omega)\overleftrightarrow{G}^{\dagger}(\boldsymbol{r}_2, \boldsymbol{r}', \omega)d^3\boldsymbol{r}'. \tag{2.5}$$

This identity ensures that at global thermal equilibrium the first kind and the second kind of FDT lead to identical results.

2.2 Thermal emission from half space uniaxial media

In this section, we consider an uniaxial medium located in the lower space ($z < 0$) at temperature T while the upper space vacuum part is at zero temperature. The relative permittivity of the uniaxial medium is a diagonal matrix, $\boldsymbol{\epsilon} = diag[\epsilon_\parallel; \epsilon_\parallel; \epsilon_\perp]$. Note that hyperbolic metamaterials are a special kind of uniaxial medium satisfying $\epsilon_\parallel\epsilon_\perp < 0$. As mentioned before, we should employ the second kind of FDT because this is a non-equilibrium problem.

To solve DGF in planar structures, it is convenient to work in the wavevector space. DGF in vacuum [5] is ($z > z'$)

$$\begin{aligned}\overleftrightarrow{G}(\boldsymbol{r}, \boldsymbol{r}', \omega) =& \frac{i}{8\pi^2}\iint \frac{dk_x dk_y}{k_{z0}} e^{i\boldsymbol{k}_\perp\cdot(\boldsymbol{r}_\perp - \boldsymbol{r}'_\perp)} \\ & \{\hat{s}^0_+\hat{s}^0_+ e^{ik_{z0}(z-z')} + \hat{p}^0_+\hat{p}^0_+ e^{ik_{z0}(z-z')}\}\end{aligned} \tag{2.6}$$

Here we define $\hat{k}_+ = (k_x, k_y, k_{z0})/k_0$ is the normalized wave-vector of upward waves ($z > z'$) in free space, $k - 0 = \omega/c$, $\boldsymbol{k}_\perp = (k_x, k_y)$, $k_\rho = \sqrt{k_x^2 + k_y^2}$, $k_{z0} = \sqrt{k_0^2 - k_\rho^2}$, and $\boldsymbol{r}_\perp = (x, y)$. $\hat{s}^0_+ = \hat{k}_+ \times \hat{z} = (k_y, -k_x, 0)/k_\rho$ is the unit direction vector of s-polarized waves, $\hat{p}^0_+ = \hat{s}^0_+ \times \hat{k}_+ = (-k_x k_{z0}, -k_y k_{z0}, k_\rho^2)/k_0 k_\rho$ is the unit direction vector of p-polarized waves. Correspondingly and for

later use, $\hat{k}_- = (k_x, k_y, -k_{z0})/k_0$ is the normalized wave-vector of downward waves (when $z < z'$), $\hat{s}^0_- = \hat{k}_- \times \hat{z} = (k_y, -k_x, 0)/k_\rho$ same with $\hat{s}^0_+$, and $\hat{p}^0_- = \hat{s}^0_- \times \hat{k}_- = (k_x k_{z0}, k_y k_{z0}, k_\rho^2)/k_0 k_\rho$.

The DGF relating thermally generated random currents inside the medium in the lower space to the fields in upper space vacuum is

$$\overleftrightarrow{G}_{01}(\boldsymbol{r}, \boldsymbol{r}') = \frac{i}{8\pi^2} \iint \frac{dk_x dk_y}{k_{z0}} e^{i\boldsymbol{k}_\perp \cdot (\boldsymbol{r}_\perp - \boldsymbol{r}'_\perp)} \{t^s \hat{s}^0_+ \hat{s}^1_+ e^{ik_{z0}z - ik_{zs}z'} + t^p \hat{p}^0_+ \hat{p}^1_+ e^{ik_{z0}z - ik_{zp}z'}\}. \tag{2.7}$$

Here, $k_{zs} = \sqrt{\epsilon_\parallel k_0^2 - k_\rho^2}$, $k_{zp} = \sqrt{\epsilon_\parallel k_0^2 - \frac{\epsilon_\parallel}{\epsilon_\perp} k_\rho^2}$, $\hat{s}^1_+ = \hat{s}^0_+ = (k_y, -k_x, 0)/k_\rho$, and $\hat{p}^1_+ = (-k_x k_{zp}, -k_y k_{zp}, k_\rho^2 \epsilon_\parallel/\epsilon_\perp)/k_0 k_\rho \sqrt{\epsilon_\parallel}$ which are the unit direction vectors of s- and p-polarized waves inside the unaxial medium, respectively. Note the transmission coefficients incident from the vacuum side should be in terms of the electric fields,

$$t^s = \frac{2k_{z0}}{k_{z0} + k_{zs}}, \quad t^p = \frac{2k_{z0}\sqrt{\epsilon_\parallel}}{\epsilon_\parallel k_{z0} + k_{zp}}. \tag{2.8}$$

To calculate the magnetic fields, we should evaluate $\nabla \times \overleftrightarrow{G}_{01}$, which can be easily done in the wavevector space. The curl operator will work on the first vector of $\overleftrightarrow{G}_{01}$,

$$\nabla \times \overleftrightarrow{G}_{01}(\boldsymbol{r}, \boldsymbol{r}') = \frac{k_0}{8\pi^2} \iint \frac{dk_x dk_y}{k_{z0}} e^{i\boldsymbol{k}_\perp \cdot (\boldsymbol{r}_\perp - \boldsymbol{r}'_\perp)} \{t^s \hat{p}^0_+ \hat{s}^1_+ e^{ik_{z0}z - ik_{zs}z'} - t^p \hat{s}^0_+ \hat{p}^1_+ e^{ik_{z0}z - ik_{zp}z'}\}. \tag{2.9}$$

The free space energy density is defined by

$$u(\omega, \boldsymbol{r}) = 2 \left(\frac{1}{2} \epsilon_0 \operatorname{Tr} \left\langle \vec{E}(\omega, \boldsymbol{r}) \otimes \vec{E}^*(\omega, \boldsymbol{r}) \right\rangle + \frac{1}{2} \mu_0 \operatorname{Tr} \left\langle \vec{H}(\omega, \boldsymbol{r}) \otimes \vec{H}^*(\omega, \boldsymbol{r}) \right\rangle \right), \tag{2.10}$$

where the prefactor 2 accounts for the negative frequency counterpart. Fol-

lowing the formalism in Ref. [87], we define

$$g_e(\boldsymbol{k}_\perp, z, z', \omega) = -\frac{1}{2k_{z0}} \left\{ t^s \hat{s}^0_+ \hat{s}^1_+ e^{ik_{z0}z - ik_{zs}z'} + t^p \hat{p}^0_+ \hat{p}^1_+ e^{ik_{z0}z - ik_{zp}z'} \right\}, \tag{2.11}$$

$$g_h(\boldsymbol{k}_\perp, z, z', \omega) = \frac{1}{2k_{z0}} \left\{ t^s \hat{p}^0_+ \hat{s}^1_+ e^{ik_{z0}z - ik_{zs}z'} - t^p \hat{s}^0_+ \hat{p}^1_+ e^{ik_{z0}z - ik_{zp}z'} \right\}. \tag{2.12}$$

One can then find

$$u(\omega, z) = \frac{\omega^3}{\pi c^4} \Theta(\omega, T) \int_{-\infty}^{0} dz' \int_{-\infty}^{+\infty} \frac{d^2\boldsymbol{k}_\perp}{4\pi^2} \left(\mathrm{Tr}\left(g_e \boldsymbol{\epsilon}'' g_e^\dagger \right) + \mathrm{Tr}\left(g_h \boldsymbol{\epsilon}'' g_h^\dagger \right) \right) \tag{2.13}$$

Inserting the expressions of g_e and g_h, we have

$$\begin{aligned} u(\omega, z) =& \frac{\omega^3}{8\pi^2 c^4} \Theta(\omega, T) e^{-2\,\mathrm{Im}(k_{z0})z} \int_{-\infty}^{0} dz' \int_{0}^{+\infty} k_\rho dk_\rho \frac{1}{|k_{z0}|^2} \left(1 + \frac{k_\rho^2 + |k_{z0}^2|}{k_0^2} \right) \\ & \left(\epsilon_\parallel'' |t^s|^2 e^{2\,\mathrm{Im}(k_{zs})z'} + \left(\frac{\epsilon_\perp'' |\epsilon_\parallel/\epsilon_\perp|^2 k_\rho^2 + \epsilon_\parallel'' |k_{zp}^2|}{k_0^2 |\epsilon_\parallel^2|} \right) |t^p|^2 e^{2\,\mathrm{Im}(k_{zp})z'} \right). \end{aligned} \tag{2.14}$$

The integration at z' can be easily done. Further by taking the imaginary part of the dispersion relation

$$\frac{k_\rho^2}{\epsilon_\parallel} + \frac{k_{zs}^2}{\epsilon_\parallel} = \frac{\omega^2}{c^2}, \quad \frac{k_\rho^2}{\epsilon_\perp} + \frac{k_{zp}^2}{\epsilon_\parallel} = \frac{\omega^2}{c^2} \tag{2.15}$$

for s- and p-polarized waves, this result can be simplified as

$$\begin{aligned} u(\omega, z) = \frac{U_{BB}(\omega, T)}{2} \Bigg\{ & \int_0^{k_0} \frac{k_\rho dk_\rho}{k_0 \left| k_{z0} \right|} \frac{(1 - |r^s|^2) + (1 - |r^p|^2)}{2} \\ & + \int_{k_0}^{\infty} \frac{k_\rho^3 dk_\rho}{k_0^3 \left| k_{z0} \right|} e^{-2\,\mathrm{Im}(k_{z0})z} (\mathrm{Im}(r^s) + \mathrm{Im}(r^p)) \Bigg\}. \end{aligned} \tag{2.16}$$

Here $U_{BB} = \frac{\omega^2}{\pi^2 c^3} \Theta(\omega, T)$ is the energy density of blackbody. r^s and r^p are the standard reflection coefficients given by

$$r^s = \frac{k_{z0} - k_{zs}}{k_{z0} + k_{zs}}, \quad r^p = \frac{\epsilon_\parallel k_{z0} - k_{zp}}{\epsilon_\parallel k_{z0} + k_{zp}}. \tag{2.17}$$

The propagating wave part $1 - |r|^2$ in Eq. (2.16) is the far field emissivity, equivalent to Kirchhoff's law. Correspondingly, the evanescent wave part can be interpreted as Kirchhoff's law in the near field and $2\,\mathrm{Im}(r)$ is the near

field emissivity [17,22,68,104], which is widely used in heat transfer problems. $2\,\mathrm{Im}(r)$ is also proportional to the near field local density of states (LDOS) proposed in Ref. [22] and is related to the tunneling and subsequent absorption of energy carried by evanescent waves. Recently extensive theoretical and experimental works have demonstrated the ability of HMMs to enhance the near field LDOS [61,63,105]. Thus we expect the use of HMMs in thermal and energy management.

2.2.1 Energy in matter and fields

We can use the above definitions to compare the energy density in the near-field of the hyperbolic metamaterials to any other control sample. A pertinent question is about how much energy density is in matter degrees of freedom as opposed to the fields. This is difficult to answer inside the medium but can be done unambiguously in the near-field.

In the high-k approximation, where the wavevector parallel to the interface k_ρ is sufficiently large, the near-field energy density is governed by the tunneling parameter which we define as the imaginary part of the p-polarized reflection coefficient. Thus studying the behavior of this tunneling parameter sheds light on the near-field energy density. In the low loss limit, the reflection for p-polarized waves incident on an interface between vacuum and HMM can be expressed by [12, 106]

$$\mathrm{Im}(r_p^{\mathrm{HMM}}) \approx \frac{2\sqrt{|\epsilon_\parallel \epsilon_\perp|}}{1+|\epsilon_\parallel \epsilon_\perp|}. \tag{2.18}$$

While for an isotropic medium, the high-k approximation gives

$$\mathrm{Im}(r_p^{\mathrm{iso}}) \approx \frac{2\epsilon''}{|1+\epsilon|^2}. \tag{2.19}$$

The most striking difference between the above equations is that for a conventional isotropic medium the near-field energy density is completely dominated by the imaginary part of the dielectric constant. These fluctuations disappear in the low loss limit and can be attributed to matter degrees of freedom. This is because the imaginary part of the dielectric constant which governs field fluctuations also characterizes the irreversible conversion of electromagnetic energy into thermal energy of matter degrees of freedom. On the other hand, the hyperbolic medium shows near-field fluctuations arising from high-k modes completely independent of material losses and the energy resides in the field.

Let us analyze what would happen at mid-infrared frequencies where phonon polaritonic materials can give rise to this low loss high-k limit for hyperbolic metamaterials. We clearly see from Eq. (2.19) that the near field emissivity would be very small when the frequency is away from the surface phonon polariton resonance (SPhPR) frequency where $\mathrm{Re}(\epsilon) = -1$. However, for HMMs made of phonon polaritonic materials and dielectrics, the near field emissivity (Eq. 2.18) can be comparably large in broad frequency region, though in this approximation its magnitude cannot exceed one. Note here we do not account for surface wave resonances which can change the picture considerably especially if one wants to optimize near-field heat transfer [106]. Our aim is to focus on the bulk modes only.

2.3 Thermal emission from multilayered structures

In this section we will consider multilayered structures. In the field of metamaterials, multilayered structures are widely used to achieve effective uniaxial media. The aim here is to go beyond effective medium theory and calculate the exact thermal emission from multilayered structures using the second kind of FDT. We assume that the medium in all layers is isotropic and non-magneto-optical for simplicity. To find DGFs relating the random currents in each layer to the vacuum region, we will follow the method in Ref. [5]. Firstly assuming the current source is in the vacuum region, we can calculate the fields induced by the source in all the layers by transfer matrix method which matches the boundary conditions at all the interfaces. Thus the DGFs with source in the vacuum region are ready to be employed. Next we use the reciprocal property of the DGF to achieve DGF when the sources are in the lower space.

DGF in the vacuum region ($z < z'$) is

$$\begin{aligned}
&\overleftrightarrow{G}_{00}(\boldsymbol{r}, \boldsymbol{r}') = \frac{i}{8\pi^2} \iint \frac{dk_x dk_y}{k_{z0}} e^{i\boldsymbol{k}_\perp \cdot (\boldsymbol{r}_\perp - \boldsymbol{r}'_\perp)} \\
&\Big\{ \left(\hat{s}^0_- e^{-ik_{z0}z} + r^s \hat{s}^0_+ e^{ik_{z0}z} \right) \hat{s}^0_- e^{ik_{z0}z'} \\
&+ (\hat{p}^0_- e^{-ik_{z0}z} + r^p \hat{p}^0_+ e^{ik_{z0}z}) \hat{p}^0_- e^{ik_{z0}z'} \Big\}
\end{aligned} \tag{2.20}$$

DGF in the intermediate slabs are

$$\begin{aligned}\overleftrightarrow{G}_{l0}(\boldsymbol{r},\boldsymbol{r}') = \frac{i}{8\pi^2}\iint \frac{dk_x dk_y}{k_{z0}} e^{i\boldsymbol{k}_\perp\cdot(\boldsymbol{r}_\perp-\boldsymbol{r}'_\perp)} \\ \Big\{ \left(B_l \hat{s}^l_- e^{-ik_{zl}z} + A_l \hat{s}^l_+ e^{ik_{zl}z}\right) \hat{s}^0_- e^{ik_{z0}z'} \\ + (D_l \hat{p}^l_- e^{-ik_{zl}z} + C_l \hat{p}^l_+ e^{ik_{zl}z}) \hat{p}^0_- e^{ik_{z0}z'} \Big\} \end{aligned} \tag{2.21}$$

DGF in the last layer is

$$\begin{aligned}\overleftrightarrow{G}_{(N+1)0}(\boldsymbol{r},\boldsymbol{r}') = \frac{i}{8\pi^2}\iint \frac{dk_x dk_y}{k_{z0}} e^{i\boldsymbol{k}_\perp\cdot(\boldsymbol{r}_\perp-\boldsymbol{r}'_\perp)} \\ \Big\{ t_s \hat{s}^t_- e^{-ik_{zt}z} \hat{s}^0_- e^{ik_{z0}z'} + t_p \hat{p}^t_- e^{-ik_{zt}z} \hat{p}^0_- e^{ik_{z0}z'} \Big\} \end{aligned} \tag{2.22}$$

Note in the last layer we only have the downward waves, namely, the transmission.

The boundary conditions give [5]

$$\begin{aligned} &A_l e^{ik_{zl}z_l} + B_l e^{-ik_{zl}z_l} = \\ &A_{l+1} e^{ik_{z(l+1)}z_l} + B_{l+1} e^{-ik_{z(l+1)}z_l} \end{aligned} \tag{2.23}$$

$$\begin{aligned} &k_{zl}(A_l e^{ik_{zl}z_l} - B_l e^{-ik_{zl}z_l}) = \\ &k_{z(l+1)}(A_{l+1} e^{ik_{z(l+1)}z_l} - B_{l+1} e^{-ik_{z(l+1)}z_l}) \end{aligned} \tag{2.24}$$

for s-polarized waves, and

$$\begin{aligned} &\sqrt{\epsilon_l}(C_l e^{ik_{zl}z_l} + D_l e^{-ik_{zl}z_l}) = \\ &\sqrt{\epsilon_{l+1}}(C_{l+1} e^{ik_{z(l+1)}z_l} + D_{l+1} e^{-ik_{z(l+1)}z_l}) \end{aligned} \tag{2.25}$$

$$\begin{aligned} &\frac{k_{zl}}{\sqrt{\epsilon_l}}(C_l e^{ik_{zl}z_l} - D_l e^{-ik_{zl}z_l}) = \\ &\frac{k_{z(l+1)}}{\sqrt{\epsilon_{l+1}}}(C_{l+1} e^{ik_{z(l+1)}z_l} - D_{l+1} e^{-ik_{z(l+1)}z_l}) \end{aligned} \tag{2.26}$$

for p-polarized waves. Following the same steps as in the uniaxial case, the final expression is

$$u(\omega,z) = \frac{\omega^3}{8\pi^2 c^4}\Theta(\omega,T)e^{-2\,\mathrm{Im}(k_{z0})z}\sum_{l=1}^{N+1}\int_{z_l}^{z_{l-1}} dz' \int_0^{+\infty} k_\rho dk_\rho$$
$$\frac{1}{|k_{z0}|^2}\left(1+\frac{k_\rho^2+|k_{z0}^2|}{k_0^2}\right)\epsilon_l''\left(\left|A_l e^{ik_{zl}z'}+B_l e^{-ik_{zl}z'}\right|^2\right.$$
$$\left.+\left|\frac{k_{zl}(C_l e^{ik_{zl}z'}-D_l e^{-ik_{zl}z'})}{k_0\sqrt{\epsilon_l}}\right|^2+\left|\frac{k_\rho(C_l e^{ik_{zl}z'}+D_l e^{-ik_{zl}z'})}{k_0\sqrt{\epsilon_l}}\right|^2\right), \quad (2.27)$$

where N is the total number of layers in the structure.

To simplify the above result, we first note that the integral

$$\int_{z_l}^{z_{l-1}} dz' k_0^2\epsilon_l''\left|A_l e^{ik_{zl}z'}+B_l e^{-ik_{zl}z'}\right|^2 =$$
$$\mathrm{Re}\left[k_{zl}(-A_l e^{ik_{zl}z}+B_l e^{-ik_{zl}z})(A_l e^{ik_{zl}z}+B_l e^{-ik_{zl}z})^*\right]\Big|_{z_l}^{z_{l-1}}$$
$$= Q_l(z_{l-1})-Q_l(z_l), \quad (2.28)$$

which is valid for all layers. From the boundary condition, we have

$$Q_l(z_l) = Q_{l+1}(z_l) \quad (2.29)$$

Thus we find

$$\sum_{l=1}^{N+1}\int_{z_l}^{z_{l-1}} dz' k_0^2\epsilon_l''\left|A_l e^{ik_{zl}z'}+B_l e^{-ik_{zl}z'}\right|^2 = Q_0(z_0)-Q_{N+1}(z_{N+1}). \quad (2.30)$$

For the last term, $z_{N+1}=-\infty$, so $Q_{N+1}(z_{N+1})=0$, and in our convention, $z_0=0$. The final result is

$$\mathrm{Re}\left[k_{z0}(1-r^s)(1+r^s)^*\right] = \begin{cases}(1-|r^s|^2)|k_{z0}|, & k_\rho < k_0\\ 2\,\mathrm{Im}(r^s)|k_{z0}|, & k_\rho > k_0\end{cases}. \quad (2.31)$$

This is the contribution from s-polarized waves. For p-polarized waves, the

corresponding identity is

$$\int_{z_l}^{z_{l-1}} dz' k_0^2 \epsilon_l'' \left(\left| \frac{k_{zl}(C_l e^{ik_{zl}z'} - D_l e^{-ik_{zl}z'})}{k_0\sqrt{\epsilon_l}} \right|^2 + \left| \frac{k_\rho(C_l e^{ik_{zl}z'} + D_l e^{-ik_{zl}z'})}{k_0\sqrt{\epsilon_l}} \right|^2 \right)$$
$$= \mathrm{Re}\left[\frac{k_{zl}}{\sqrt{\epsilon_l}}(C_l e^{ik_{zl}z} - D_l e^{-ik_{zl}z}) \ (\sqrt{\epsilon_l}(C_l e^{ik_{zl}z} + D_l e^{-ik_{zl}z}))^* \right] \Big|_{z_l}^{z_{l-1}} \tag{2.32}$$

Then the contribution from p-polarized waves can be evaluated in the similar way. The final expression for thermal emission from a half space multilayered structure will be given by Eq. (2.16). The reflection coefficients should be that of the whole structure.

If we are interested in a slab inside vacuum rather than a half space structure, we can eliminate the contribution from the last layer vacuum part. To do so, in Eq. (2.28), for the last layer $A_{N+1} = 0$ and $B_{N+1} = t^s$, the right hand side is therefore $\mathrm{Re}(k_{z0})|t^s|^2$, which vanishes for evanescent waves. Subtracting this term from Eq. (2.16) gives the thermal emission from a multilayered slab inside vacuum,

$$u(\omega, z) = \frac{U_{BB}(\omega, T)}{2}$$
$$\left\{ \int_0^{k_0} \frac{k_\rho dk_\rho}{k_0 |k_{z0}|} \frac{(1 - |r^s|^2 - |t^s|^2) + (1 - |r^p|^2 - |t^p|^2)}{2} \right.$$
$$\left. + \int_{k_0}^{\infty} \frac{k_\rho^3 dk_\rho}{k_0^3 |k_{z0}|} e^{-2\,\mathrm{Im}(k_{z0})z} (\mathrm{Im}(r^s) + \mathrm{Im}(r^p)) \right\}. \tag{2.33}$$

The above expression can be also obtained by replacing $1 - |r|^2$ in Eq. (2.16) with $1 - |r|^2 - |t|^2$, which is consistent with Kirchoff's law.

2.4 Scattering matrix method and spatial coherence

We now describe another approach to evaluating the near-field energy density near metamaterials using the scattering matrix approach. However, first we will discuss a few important points related to the concept of the thermal environment. We note that when the lower space is vacuum, the reflection coefficients are zero. As a result of Eq. (2.16), the contribution from the evanescent waves part is zero while that from the propagating waves is nonzero. However,

this is not very intuitive from FDT. The reason is that losses of vacuum i.e. ϵ'' of vacuum is zero and from the second kind of FDT, the correlation function of random currents of vacuum should be zero, suggesting a zero field correlation. It turns out that for an unbounded vacuum region, we should add an infinitesimal imaginary part to ϵ_0, integrate over the region and then take the limit of the imaginary part to be zero in the final expression [37, 107]. This is needed to preserve causality requirements. In the derivation of Eq. (2.16), we have integrated the source region z' from $-\infty$ to 0. However, for a vacuum gap with any finite width, the final fields correlation originating from the gap can be shown to be zero [3]. For this reason, fluctuations in vacuum can be interpreted to come from infinity.

It is then natural to think about the thermal emission from the upper space vacuum region as well. If the vacuum region is also at temperature T, the system is at global thermal equilibrium. Therefore we can employ the first kind of FDT to calculate the thermal energy density. This approach is used in Ref. [108] to define the local density of states. Here we directly cite the final result,

$$\begin{aligned} u_{eq}(z,\omega,T) &= \frac{U_{BB}(\omega,T)}{2} \\ &\left\{ \int_0^{k_0} \frac{k_\rho dk_\rho}{k_0 \left|k_{z0}\right|} \left(2 + \frac{k_\rho^2}{k_0^2}[\mathrm{Re}(r^s e^{2ik_{z0}z}) + \mathrm{Re}(r^p e^{2ik_{z0}z})]\right) \right. \\ &\left. + \int_{k_0}^{\infty} \frac{k_\rho^3 dk_\rho}{k_0^3 \left|k_{z0}\right|} e^{-2\,\mathrm{Im}(k_{z0})z} (\mathrm{Im}(r^s) + \mathrm{Im}(r^p)) \right\} \end{aligned} \tag{2.34}$$

Note again that the contribution from evanescent waves equals that of Eq. (2.16), implying no evanescent waves contribution from the upper space vacuum region. However, in non-equilibrium, to determine electromagnetic fields induced by every random current inside the medium using second kind of FDT is quite laborious. We note from the second kind of FDT that the currents are not spatially correlated, which suggests that the thermal emission from different spatial regions can be calculated separately. In thermal equilibrium, we can calculate the thermal energy density by the first kind of FDT. Thus if we can calculate the thermal emission from the upper space vacuum part at temperature T, thermal emission only from the lower space can be achieved by excluding the vacuum part from the total thermal energy density.

The electric field generated by the upper half vacuum space can be written

as [43]

$$\vec{E}_f(\omega, \boldsymbol{r}) = \int \frac{d^2\boldsymbol{k}_\perp}{4\pi^2} \vec{E}_f(\omega, \boldsymbol{k}_\perp, z) e^{i\boldsymbol{k}_\perp \cdot \boldsymbol{r}_\perp} \tag{2.35}$$

where

$$\vec{E}_f(\omega, \boldsymbol{k}_\perp, z) = (a_s(\omega, \boldsymbol{k}_\perp)\hat{s}^0_- + a_p(\omega, \boldsymbol{k}_\perp)\hat{p}^0_-) e^{-ik_{z0}z}. \tag{2.36}$$

a_s and a_p are the field amplitude for s and p-polarized waves, respectively. The operator $a = (a_s, a_p)^T$ satisfies the correlation function [43],

$$\left\langle a(\omega, \boldsymbol{k}_\perp) \otimes a^\dagger(\omega', \boldsymbol{k}'_\perp) \right\rangle = 4\pi^2 C(\omega, \boldsymbol{k}_\perp)\delta(\omega - \omega')\delta^2(\boldsymbol{k}_\perp - \boldsymbol{k}'_\perp). \tag{2.37}$$

The coefficient C can be read directly from FDT and the free space DGF,

$$C(\omega, k_\perp) = \frac{\mu_0 \omega}{4\pi} \Theta(\omega, T)\, \mathrm{Re}\,(\frac{1}{k_{z0}}), \tag{2.38}$$

which vanishes for evanescent waves. These fluctuations from the upper vacuum region shines on the interface and get reflected. The total fields due to fluctuations in the vacuum part are

$$\begin{aligned} \vec{E}_0(z,\omega, \boldsymbol{k}_\perp) = &(a_s(\omega, \boldsymbol{k}_\perp)s^0_- + a_p(\omega, \boldsymbol{k}_\perp)p^0_-) e^{-ik_{z0}z} \\ &+ (r^s a_s(\omega, \boldsymbol{k}_\perp)s^0_+ + r^p a_p(\omega, \boldsymbol{k}_\perp)p^0_+) e^{ik_{z0}z}. \end{aligned} \tag{2.39}$$

The magnetic fields can be calculated using Eq. (2.39) and Maxwell equations. Then one can find the energy density due to the fluctuations in the upper space vacuum,

$$\begin{aligned} u_0(z, \omega, T) = &\frac{U_{BB}(\omega, T)}{2} \int_0^{k_0} \frac{k_\rho dk_\rho}{k_0 |k_{z0}|} \Big\{ 1 + \\ &\frac{|r^s|^2 + |r^p|^2}{2} + \frac{k_\rho^2}{k_0^2} [\mathrm{Re}(r^s e^{2ik_{z0}d}) + \mathrm{Re}(r^p e^{2ik_{z0}d})] \Big\} \end{aligned} \tag{2.40}$$

Subtracting Eq. (2.40) from Eq. (2.34), we recover the expression by the second kind of FDT.

From the definition of the cross-spectral density tensor

$$W(\boldsymbol{r}_1, \boldsymbol{r}_2, \omega)\delta(\omega - \omega') = \left\langle \vec{E}(\boldsymbol{r}_1, \omega) \otimes \vec{E}^*(\boldsymbol{r}_2, \omega') \right\rangle, \tag{2.41}$$

one can find the spatial coherence due to fluctuations in the upper space vac-

uum,

$$W^0_{zz}(\boldsymbol{r}_1,\boldsymbol{r}_2,\omega) = \frac{U_{BB}(\omega,T)}{4\epsilon_0}\int_0^{k_0}\frac{k_\rho^3 dk_\rho}{k_0^3|k_{z0}|}J_0(k_\rho d) \left[\frac{1+|r^p|^2}{2}+\mathrm{Re}(r^p e^{2ik_{z0}d})\right] \tag{2.42}$$

where $\boldsymbol{r}_1 = (0,0,z)$, $\boldsymbol{r}_2 = (d,0,z)$ and $\int_0^{2\pi} d\theta e^{ik_\rho d\cos\theta} = 2\pi J_0(k_\rho d)$ is used; $J_0(k_\rho d)$ is the zeroth order Bessel function of the first kind. Further, from Eq. (2.1), the first kind of FDT, we have

$$W^{eq}_{zz}(\boldsymbol{r}_1,\boldsymbol{r}_2,\omega) = \frac{U_{BB}(\omega,T)}{4\epsilon_0}\Big\{\int_0^{k_0}\frac{k_\rho^3 dk_\rho}{k_0^3|k_{z0}|}J_0(k_\rho d)\left[1+\mathrm{Re}(r^p e^{2ik_{z0}d})\right] + \int_{k_0}^{\infty}\frac{k_\rho^3 dk_\rho}{k_0^3|k_{z0}|}J_0(k_\rho d)\,\mathrm{Im}(r^p)e^{-2\,\mathrm{Im}(k_{z0})z}\Big\} \tag{2.43}$$

Then the contribution from the lower space structure is

$$W_{zz}(\boldsymbol{r}_1,\boldsymbol{r}_2,\omega) = \frac{U_{BB}(\omega,T)}{4\epsilon_0}\Big\{\int_0^{k_0}\frac{k_\rho^3 dk_\rho}{k_0^3|k_{z0}|}J_0(k_\rho d)\frac{1-|r^p|^2}{2} + \int_{k_0}^{\infty}\frac{k_\rho^3 dk_\rho}{k_0^3|k_{z0}|}J_0(k_\rho d)\,\mathrm{Im}(r^p)e^{-2\,\mathrm{Im}(k_{z0})z}\Big\} \tag{2.44}$$

Only p-polarized waves contributes to W_{zz} since s-polarized waves do not have E_z components.

Once again, if the structure is a multilayered slab in vacuum, the contribution from the lower vacuum space can be evaluated using the scattering matrix method in a similar way to the upper vacuum space. The fields due to the vacuum fluctuations in the lower space transmit through the planar structure,

$$\vec{E}_t(\omega,\boldsymbol{k}_\perp,z) = (t^s a_s(\omega,\boldsymbol{k}_\perp)\hat{s}^0_- + t^p a_p(\omega,\boldsymbol{k}_\perp)\hat{p}^0_-)e^{ik_{z0}z}. \tag{2.45}$$

It is clear that the contributing energy density will be proportional to the $|t|^2$, so that we recover the result of Eq. (2.33). Note that due to the reciprocal property, the transmission coefficients from two sides of the structure should be identical.

Generally speaking, considering a single object in thermal equilibrium, the energy density can be determined by the first kind of FDT, which is simply a single scattering event. To find the contribution from the object only, we can exclude the contribution from the environment, which can be also expressed

by the scattering matrix of the object. If there are several objects at different temperatures, we can first decide the thermal emission from one specific object in the absence of other objects and then build the scattering part from other objects, in which procedure the temperatures of the other objects and the environment are assumed to be zero. Note this is the basic idea of M. Kardar and co-authors in sequent works [36, 37, 109]. Beyond the multilayered structures considered here, the authors also give the scattering matrix of various geometries including sphere and cylinder. For more complicated objects, numerical methods are also well developed [46, 47, 110, 111].

2.5 Heat transfer

The heat transfer between two plates separated by a vacuum gap at different temperatures can be found through computing the Poynting vector inside the gap. One can first find the fields on the interface of each plate assuming the other plate is absent, which structure is just the half space problem we have discussed. Then the fields on the interface of each plate can be seen as the boundary condition of the fields inside the gap. Next we can simply employ the plane wave expansion to compute the fields inside the gap and finally obtain the Poynting vector [20, 21].

We consider two homogeneous half-space mediums (labeled by 1 and 2) separated by a vacuum gap with width d. One medium is at local equilibrium with T_1 and the other with T_2. Within the framework of Rytov's fluctuational electrodynamics, Polder and Van Hove [7] first derived the general expressions of the heat flux between the two media

$$\begin{aligned}\mathrm{H}(d,T_1,T_2) &= \int_0^\infty \frac{d\omega}{2\pi}\hbar\omega(n(\omega,T_1)-n(\omega,T_2)) \\ &= \sum_{j=s,p}\left\{\int_0^{k_0}\frac{d^2k_\parallel}{4\pi^2}\frac{(1-\left|r_j^{01}\right|^2)(1-\left|r_j^{02}\right|^2)}{\left|1-r_j^{01}r_j^{02}e^{2ik_zd}\right|^2}\right. \\ &\left. + \int_{k_0}^\infty \frac{d^2k_\parallel}{4\pi^2}e^{-2\,\mathrm{Im}(k_z)z}\frac{4\,\mathrm{Im}(r_j^{01})\,\mathrm{Im}(r_j^{02})}{\left|1-r_j^{01}r_j^{02}e^{2ik_zd}\right|^2}\right\}. \end{aligned} \tag{2.46}$$

Here, $\Theta(\omega,T) = \hbar\omega n(\omega,T)$ is the mean energy of a harmonic oscillator, $n(\omega,T) = 1/(\exp(\hbar\omega/k_BT)-1)$ is the Bose-Einstein occupation number, $k_0 = \omega/c$ is the free space wave-vector, $k_\parallel = (k_x,k_y)$, $k_\rho = \sqrt{k_x^2+k_y^2}$, $k_z =$

$\sqrt{k_0^2 - k_\parallel^2}$, $j = s, p$ accounts for the s and p polarizations, r_j^{0i} are the Fresnel reflection coefficients between vacuum (labeled by 0) and the medium ($i = 1, 2$) for s and p waves. The contribution of propagating waves ($k_\parallel < k_0$) and evanescent waves ($k_\parallel > k_0$) are naturally separated in this expression. The propagating wave term is Kirchhoff's law taking the multiple reflections into account. Here $2\,\mathrm{Im}(r_j^{0i})$ in the evanescent waves term can be interpreted as the generalization of emissivity to the near field [17, 104]. We note $2\,\mathrm{Im}(r_j^{0i})$ are also proportional to the near field local density of states (LDOS) proposed by Pendry [22] and is related to the tunneling and subsequent absorption of energy carried by evanescent waves. Recent work has shown that the heat flux between two planar structures just depends on the scattering matrix, regardless of the inner structure of the half space medium [43]. We utilize this approach for planar multilayer HMMs. The broadband enhancement in the near field LDOS of HMMs can be utilized to engineer the heat transfer at the nanoscale [72, 105]. We will use both the approximate effective medium theory and the exact Bloch theorem to calculate the reflection coefficients and compare the heat transfer properties of HMMs.

To clearly understand the physical meaning of the above expression for heat transfer [38], we define that η is the absorptivity/emissivity of a plate, since emissivity should equal absorptivity from Kirchhoff's law,

$$\eta = \begin{cases} 1 - |r|^2, \text{ PWs} \\ 2\,\mathrm{Im}(r), \text{ EWs} \end{cases} . \tag{2.47}$$

Here 'PWs' denotes propagating waves and 'EWs' denotes evanescent waves. The number of photon emitted by plate 1 is $N_1 = n_1(\omega, T_1)\eta_1$. The emitted waves propagate within the gap with a factor $e^{ik_z d}$. At the second plate they get partially absorbed and partially reflected. Thus the number of photon emitted by plate 1 and then directly absorbed by plate 2 is

$$N_{1\to 2}^{1st} = n_1(\omega, T_1)|e^{ik_z d}|^2\eta_1\eta_2. \tag{2.48}$$

Likewise, the number of photon emitted by plate 2 and then directly absorbed by plate 1 is

$$N_{2\to 1}^{1st} = n_2(\omega, T_2)|e^{ik_z d}|^2\eta_2\eta_1. \tag{2.49}$$

Therefore the number of photons exchanged directly from plate 1 to plate 2 is

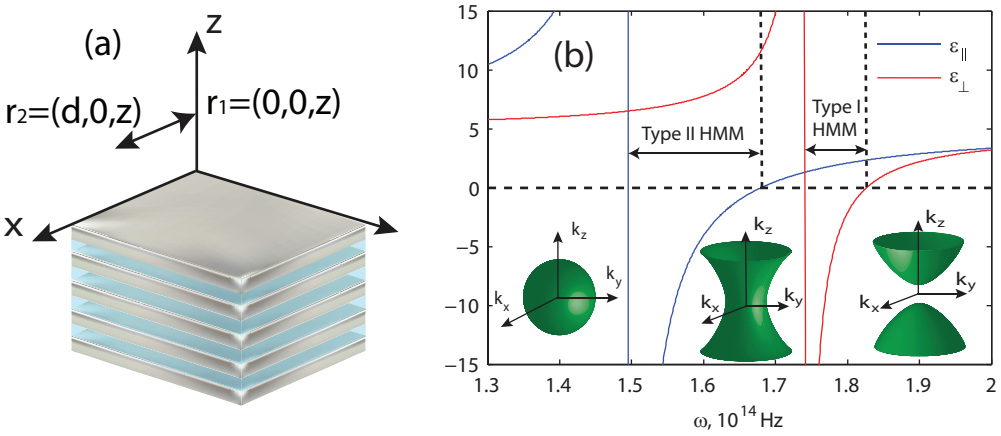

Figure 2.1: (a) Schematic of the multilayered structure and the coordinates. The spatial coherence are calculated between $\boldsymbol{r}_1 = (0, 0, z)$ and $\boldsymbol{r}_2 = (d, 0, z)$. (b) Effective permittivities of a SiO_2-SiC multilayered structure, where the fill fraction of SiC is 0.4. Only real part of the permittivity is plotted. The insets from left to right, denote the iso-frequency dispersion of dielectric, type II HMM and type I HMM.

$$N^{1st}_{1\to 2} - N^{1st}_{2\to 1} = (n_1(\omega, T_1) - n_2(\omega, T_2))|e^{ik_z d}|^2 \eta_1 \eta_2. \tag{2.50}$$

Next we incorporate the factor $1/(1 - r_1 r_2 e^{2ik_z d})$ which accounts for the multi-reflection between the two plates, and get the total number exchanged between the two plates,

$$N = N_{1\to 2} - N_{2\to 1} = (n_1(\omega, T_1) - n_2(\omega, T_2)) \frac{|e^{ik_z d}|^2}{|1 - r_1 r_2 e^{2ik_z d}|^2} \eta_1 \eta_2. \tag{2.51}$$

Lastly, $\hbar\omega N$ is just the energy exchanged (heat transfer) between the two plates. Thus we reproduce the main expression for heat transfer, which is usually derived by starting from FDT, within the simple photon exchange picture.

2.6 Results and discussions

There are multiple approaches to achieving hyperbolic dispersion [61,62]. Two of the prominent geometries consists of 1D or 2D periodic metal-dielectric structures. We consider here a multilayer combination of silicon dioxide (SiO_2) and silicon carbide (SiC) which has a metallic response in the Reststrahlen

band due to phonon polaritons ($\mathrm{Re}(\epsilon) < 0$ between $\omega_{TO} = 149.5 \times 10^{12}$ Hz and $\omega_{LO} = 182.7 \times 10^{12}$ Hz, the transverse and longitudinal optical phonon resonance frequencies). The permittivity of SiC is given by $\epsilon_m = \epsilon_\infty(\omega_{LO}^2 - \omega^2 - i\gamma\omega)/(\omega_{TO}^2 - \omega^2 - i\gamma\omega)$, where ω is the frequency of operation, $\omega_\infty = 6.7 \times 10^{12}$ Hz and $\gamma = 0.9 \times 10^{12}$ Hz. We note that this realization formed the testbed for the first complete characterization of the modes of hyperbolic metamaterials due to their low loss as compared to plasmonic media [80]. The modes of this HMM can be excited at relatively lower temperatures (400-500K) when the peak of black body emission lies within the Reststrahlen band of SiC.

To understand the thermal properties of phonon-polaritonic hyperbolic metamaterials we need to focus only on the Reststrahlen band of SiC where it is metallic. The multilayer structure (see schematic in Fig. 2.1(a)) shows a host of different electromagnetic responses as predicted by effective medium theory $\epsilon_\parallel = \epsilon_m f + \epsilon_d(1-f)$ and $\epsilon_\perp = \epsilon_m\epsilon_d/(\epsilon_d f + \epsilon_m(1-f))$, here f is the fill fraction of the metallic medium [61].

We classify the effective uniaxial medium [61, 62] using the isofrequency surface of extraordinary waves which follow $k_z^2/\epsilon_\parallel + (k_x^2 + k_y^2)/\epsilon_\perp = \omega^2/c^2$ and the media are hyperboloidal only when $\epsilon_\parallel\epsilon_\perp < 0$. We can effectively achieve a type I hyperbolic metamaterial with only one negative component in the dielectric tensor ($\epsilon_\parallel > 0$, $\epsilon_\perp < 0$), type II hyperbolic metamaterial with two negative components ($\epsilon_\parallel < 0$, $\epsilon_\perp > 0$), effective anisotropic dielectric ($\epsilon_\parallel > 0$, $\epsilon_\perp > 0$) or effective anisotropic metal ($\epsilon_\parallel < 0$, $\epsilon_\perp < 0$). In Fig. 2.1(b), we plot the effective permittivities of a SiO_2-SiC multilayered structure with the fill fraction 0.4 and label the two hyperbolic regions. As the purpose of this work is to examine how extraordinary waves in HMMs impact thermal emission properties, we only consider p-polarized waves in our numerical simulations.

2.6.1 Far field thermal emission

We first characterize the thermal emission of a HMM slab in the far field. This is extremely important for experiments currently being pursued in multiple groups. We clearly observe two peaks in Fig. 2.2 in agreement with the previous work on epsilon-near-zero and epsilon-near-pole resonances for thermal emission [81]. The right one occurs when $\epsilon_\perp$ is close to zero. From the displacement field boundary condition, $\epsilon_0 E_{0\perp} = \epsilon_\perp E_{1\perp}$, when $\epsilon_\perp \to 0$, the fields inside HMM $E_{1\perp}$ should be very large. Thus large absorption is ex-

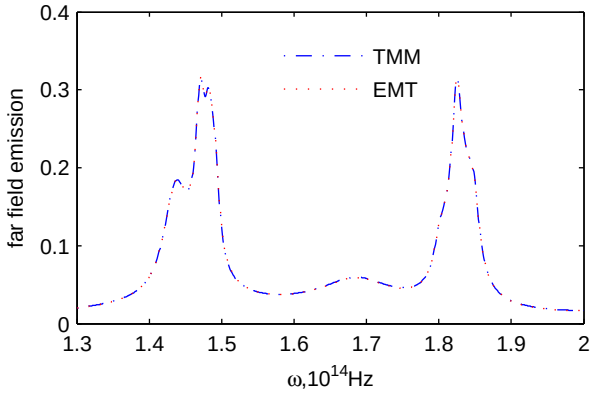

Figure 2.2: Far field thermal emission (normalized to blackbody emission) of a 3μm SiO_2-SiC multilayered structure, where fill fraction of SiC is 0.4.

pected at this epsilon-near-zero (ENZ) region. The epsilon-near-pole (ENP) resonance results in narrowband thermal emission due to the increase in the imaginary part of the dielectric constant in this ENP spectral region. The most critical aspect is the direction of the dielectric tensor components which show ENZ or ENP [81]. An ENZ in the component parallel to the interface or an ENP perpendicular to the interface does not show such effects.

2.6.2 Near field thermal emission

Here we analyze the near-field thermal emission from multilayer hyperbolic metamaterials [12]. We first focus on how thermal emission will depend on the thickness of the slabs. In Fig. 2.3, we plot the wavevector resolved thermal emission from a structure consists of 40 layers of SiO_2/SiC , 30nm/20nm achieving a net thickness of 1μm. We clearly see multiple discrete high-k modes in both the type I and type II hyperbolic region. Note the thickness 1μm is about one tenth of the operating wavelength, so these high-k modes will not occur in conventional isotropic dielectrics. The excellent agreement between the EMT prediction and the practical multilayered structure is seen, which validates the use of EMT in our structure. Further, we increase the thickness of the slab to 3μm and 30μm while keeping the same unit cell. The waveguide modes will be denser as expected. At the thickness of 30μm, the high-k modes are almost continuous and result in two bright bands in Fig. 2.4(b). This is close to the bulk metamaterial limit.

We show the thermal emission spectrum in Fig. 2.5(a) for various thick-

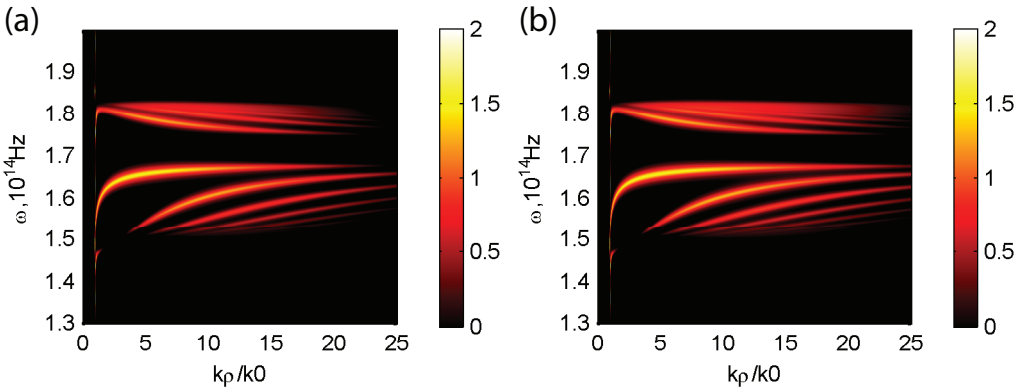

Figure 2.3: Wavevector resolved thermal emission (normalized to blackbody emission into the upper space) from a SiO_2-SiC multilayered structure calculated by (a) transfer matrix method and (b) EMT at z=200nm. The thermal emission is normalized to the black body emission to the upper half-space and in log scale. The structure consists of 40 layers of SiO_2/SiC , 30nm/20nm achieving a net thickness of 1μm. The presence of high-k modes are clearly evident in both the EMT calculation and the multilayer practical realization which takes into account all non-idealities due to dispersion, losses, finite unit cell size and finite sample size. The bright curves denote the enhanced thermal emission due to high-k modes in the HMM. In the practical multilayered structure, the high-k modes come from the coupled short range surface phonon polaritons at the silicon carbide and silicon dioxide interfaces.

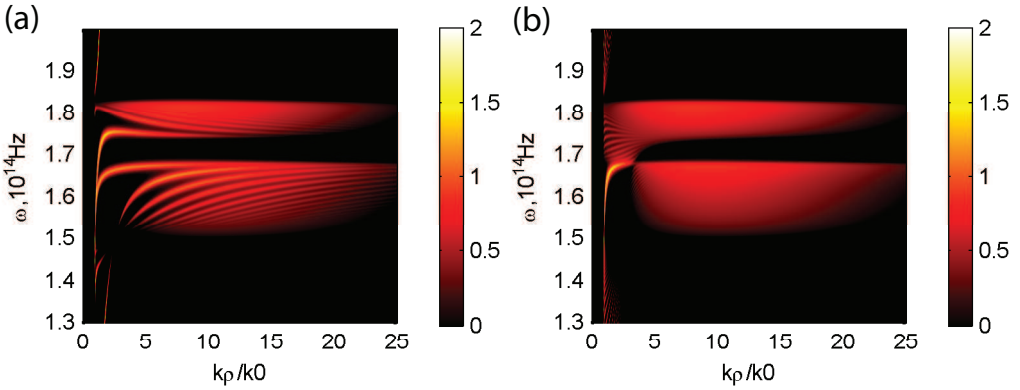

Figure 2.4: Wavevector resolved thermal emission (normalized to blackbody emission into the upper space) from (a) a 3μm thickness HMM slab and (b) a 30μm thickness HMM slab. The fill fraction of SiC is 0.4, same as the 1μm HMM slab. The two hyperbolic regions where the thermal emission is enhanced are evident. The modes supported by 3μm thickness slab are denser than that of 1μm slab and the modes supported by the 30μm slab are almost continuous.

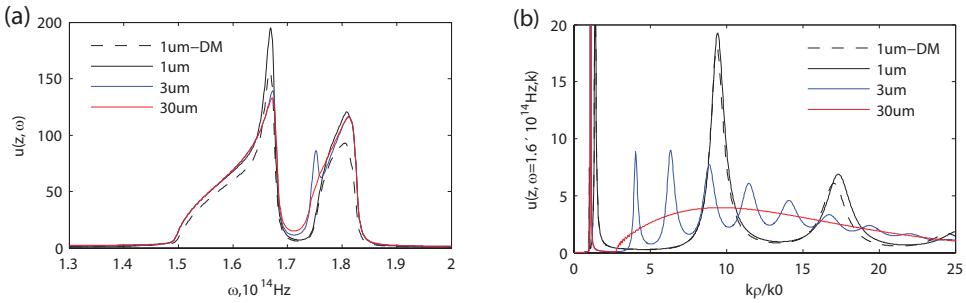

Figure 2.5: (a) Thermal emission (normalized to blackbody emission) from slabs with various thicknesses. The dashed black line is calculated using transfer matrix method while the solid lines are calculated using EMT parameters, where 'DM' in the legend means the top layer of SiO_2(Dielectric)-SiC(Metal) multilayers is SiO_2. Despite the clear difference of the density of modes supported by the slabs shown in Fig. 2.3 and 2.4, the thermal emission spectrum are interestingly in good agreement. The two main peaks where the thermal emission are largely enhanced are due to the high-k states in the two hyperbolic regions. (b) Wavevector resolved thermal emission at $\omega = 1.6 \times 10^{14}$Hz. The sharp peaks on the left ($k_\rho/k_0 < 2$) are the surface modes. When $k_\rho/k_0 > 3$, the curve for 30μm slab is almost flat with no oscillations, while that of 1μm and 3μm slabs show the discrete modes denoted by crests and troughs.

nesses of the metamaterial. The two main peaks are due to the high-k modes in the hyperbolic region. In Fig. 2.5(b), we plot the wavevector resolved thermal emission at a specific frequency $\omega = 1.6 \times 10^{14}$Hz within the type II hyperbolic region where the structure supports both surface mode and high-k modes. The sharp peaks at the left are due to the surface mode while the high-k modes emerge at larger k_ρ. In the high-k modes region, the curve for 30μm slab is almost flat indicative of a continuum of high-k modes. In contrast, the curves of 1μm and 3μm slabs clearly show the existence of discrete high-k waveguide modes featured by crests and troughs.

2.6.3 Spatial coherence of hyperbolic metamaterial slab

Surface waves can lead to large spatial coherence length in the near field [84]. To see this, we first show in Fig. 2.6 the wavevector resolved thermal emission from a 30μm thick SiC slab. The bright curve gives the dispersion of surface phonon polariton (SPhP) between the vacuum and SiC interface. Note we will not see the splitting of the vacuum-SiC interface SPhP mode into long range and short range modes since 30μm is in the order of several operating wavelengths. In the time domain, the temporal coherence is best for monochromatic

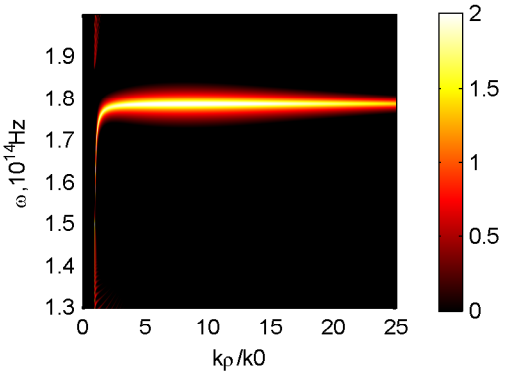

Figure 2.6: Thermal emission from a 30μm SiC slab. The red bright curve represents the dispersion of the SPhP mode between the vacuum and SiC interface since the slab is very thick.

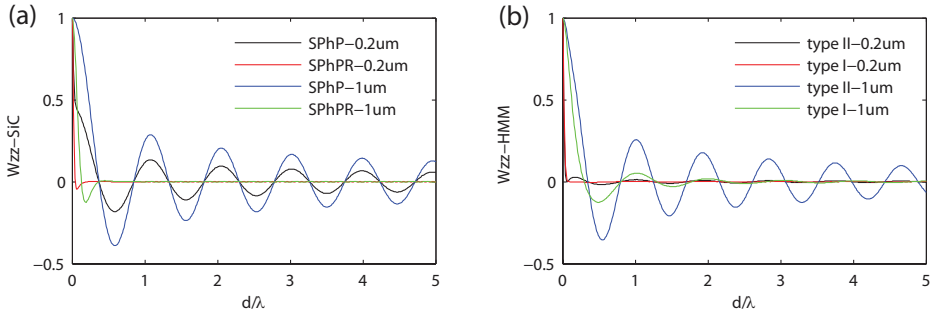

Figure 2.7: Spatial coherence of (a) a 30μm SiC slab and (b) a 30μm HMM slab at 0.2μm and 1μm from the surface with $\omega = 1.6 \times 10^{14}$Hz and $\omega = 1.79 \times 10^{14}$Hz. (a) At $\omega = 1.6 \times 10^{14}$Hz, the SiC slab supports a single degenerate SPhP mode. As a result, SiC slab has large spatial coherence at both 0.2μm and 1μm. At $\omega = 1.79 \times 10^{14}$Hz, the SPhP resonance frequency where $\mathrm{Re}\,\epsilon_{\mathrm{SiC}} = -1$, this frequency corresponds to a bright horizontal line in the SPhP dispersion curve shown in Fig. 2.6. This means at this frequency, multi-modes with different wavevectors can be thermally excited. Thus the spatial coherence is poor both at 0.2μm and 1μm. (b)At $\omega = 1.6 \times 10^{14}$Hz, the HMM slab supports high-k states besides the SPhP mode. At 0.2μm, the high-k states contribute a lot to the fluctuating electric fields, and consequently the spatial coherence is poor. But when the distance becomes larger at 1μm, the high-k states will not reach that far because of their large wavevector k_ρ. Thus the electric fields will be dominated by the surface mode which has smaller k_ρ. The spatial coherence length is large due to this dominant surface mode. At $\omega = 1.79 \times 10^{14}$Hz, the HMM slab can only supports multiple high-k states, and unlike the type II HMM region, there is no lower bound for the high-k wavevectors. Thus the spatial coherence is poor both at 0.2μm and 1μm.

waves. Thus for the spatial coherence, one can imagine it will be favorable if a single wavevector dominates the fields among all the wavevectors. This is indeed the case for surface waves. In Fig. 2.7(a), we plot the spatial coherence of the SiC slab at $\omega = 1.6 \times 10^{14}$Hz and $\omega = 1.79 \times 10^{14}$Hz. At the frequency $\omega = 1.6 \times 10^{14}$Hz, the SPhP mode wavevector k_ρ is about $1.1k_0$. Large spatial coherence length is seen at both 0.2μm and 1μm from the interface. However, near the surface phonon polariton resonance (SPhPR) frequency $\omega = 1.79 \times 10^{14}$Hz where $\epsilon_{\text{SiC}} = -1$, the mode dispersion curve is almost a horizontal line, which means that multiple modes with different wavevectors can be thermally excited. Thus a poor spatial coherence is expected. In Fig. 2.7(a), the spatial coherence is poor at at both 0.2μm and 1μm from the interface. This feature could be used to determine the resonance frequency.

Hyperbolic metamaterials can support multiple high-k modes. Therefore the spatial coherence length should not be long in the hyperbolic region. This is true for type I HMM. In Fig. 2.7(b), we plot W_{zz} at $\omega = 1.79 \times 10^{14}$Hz, where the multilayered structure effectively behaves in the type I hyperbolic region. The spatial coherence lengths are only a fraction of the operating wavelength at both 0.2μm and 1μm from the interface.

But the situation for type II hyperbolic region is interestingly different. For a HMM slab in the type II hyperbolic region ($\epsilon_\parallel < 0$, $\epsilon_\perp > 0$), the slab can support a surface wave mode as well as multiple high-k modes. Thus we have two sets of modes that can result in a unique interplay of spatial coherence effects. Furthermore, these modes are separated in wavevector space because of the lower bound of the high-k states in type II hyperbolic region [61]. High-k modes are confined to the surface better than suface waves and these high-k waves will dominate at a shorter distance from the interface. We choose $\omega = 1.6 \times 10^{14}$Hz within the type II hyperbolic region to confirm this point. At distance 0.2μm, the spatial coherence is very poor. However, at a larger distance 1μm, the fluctuating fields have large spatial coherence length. This is because at this distance, the contribution from surface wave mode dominates the electric fields while the high-k states rarely contribute to the fields. This distance dependence behavior can have applications such as obtaining the modes distribution at a given frequency.

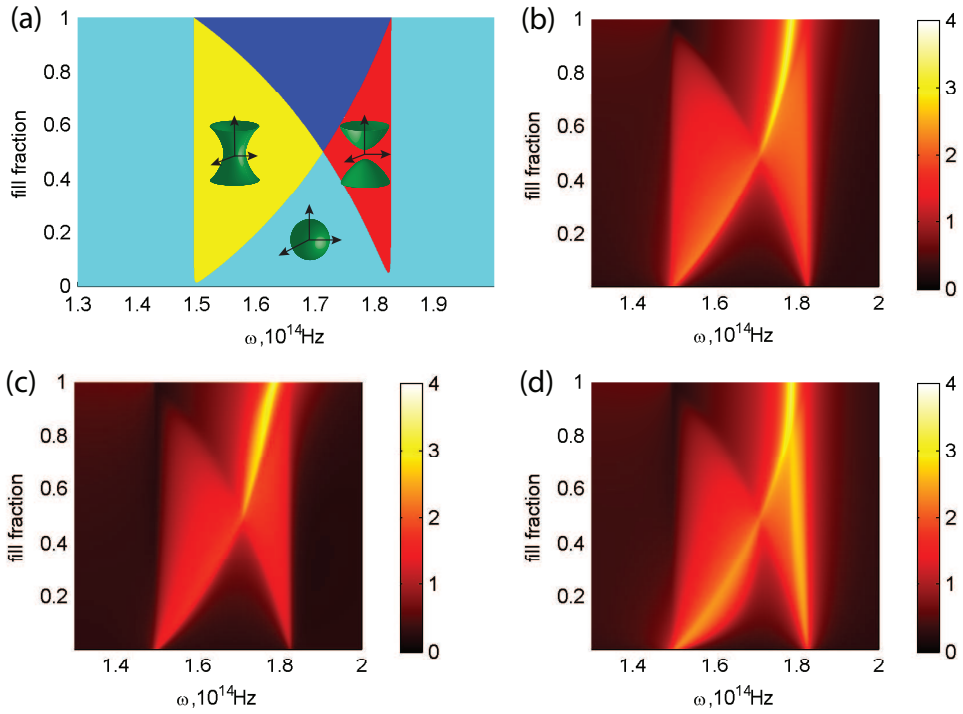

Figure 2.8: (a) Optical phase diagram of SiC-SiO_2 multilayered structure predicted by EMT. Cyan region denotes effective dielectric, blue region means effective metal, red region stands for type I hyperbolic metamaterial, yellow region is type II hyperbolic metamaterial. Thermal emission at z=200nm (log scale plot normalized to the black body radiation into the upper half-space) by the multilayered structure depending on the operating frequency and the fill fraction calculated by (b) EMT, (c) SiO_2-SiC multilayer (with first layer SiO_2), (d) SiC-SiO_2 multilayer (with first layer SiC). In the effective metal region, the dark red line is due to surface phonon polariton resonance. Both type I and type II region have a clear thermal emission enhancement due to bulk high-k modes in agreement with the optical phase diagram.

2.6.4 Thermal topological transitions

Until now, we have fixed the fill fraction to be 0.4. It is useful to examine the structure's behavior at various fill fractions. In Fig. 2.8(a), we plot the optical phase diagram [12, 61] of this metamaterial which shows the isofrequency surfaces achieved at different frequencies and fill fractions of SiC. The phase diagram is classified as effective dielectric, effective metal, type I and type II HMM as introduced before [61, 62].

Figure. 2.8(b) shows the thermal energy density (normalized to black body radiation into the upper half space) evaluated using Rytov's fluctuational electrodynamics for an effective medium slab at a distance of z=200nm from the metamaterial. It is seen that the regions of hyperbolic behavior exhibit super-Planckian thermal emission in agreement with our previous analytical approximation, but here we will go beyond effective medium theory and consider practical structures. The role of the surface waves is very important and can lead to significant deviations when the unit cell size is not significantly sub-wavelength [68, 79, 82].

The macroscopic homogenization utilized to define a bulk electromagnetic response is valid when the wavelength of operation exceeds the unit cell size ($\lambda \gg a$). However, even at such wavelengths if one considers incident evanescent waves on the metamaterial the unit cell microstructure causes significant deviations from EMT. This is an important issue to be considered for quantum and thermal applications where the near-field properties essentially arise from evanescent wave engineering (high-k modes) [61, 62]. For the multilayer HMM, at distances below the unit cell size, the thermal emission is dominated by evanescent waves with lateral wavevectors $k_\rho \gg 1/a$. Since this is above the unit-cell cut off of the metamaterial, the high-k modes do not contribute to thermal emission at such distances. It is therefore necessary to consider thermal emission from a practical multi-layer structure taking into account the layer thicknesses. This is shown in Fig. 2.8(c) and Fig. 2.8(d). The unit cell size is 200nm, and we consider a semi-infinite multilayer medium using the formalism outlined in Ref. [79]. An excellent agreement is seen of the optical phases of the multilayer structure with the EMT calculation.

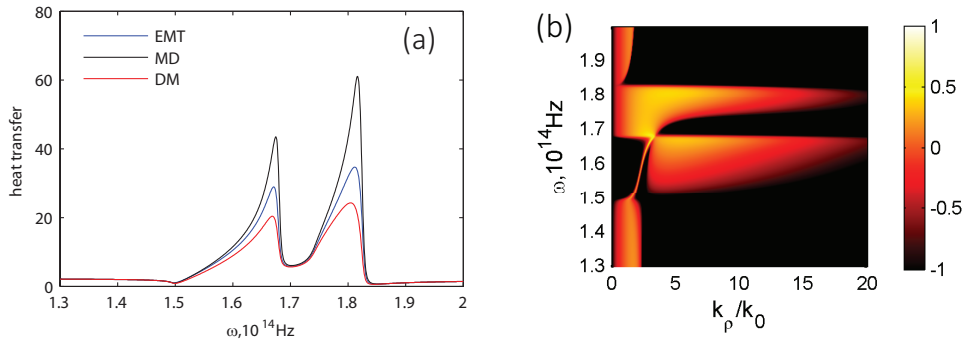

Figure 2.9: (a) Heat transfer spectrum (normalized to heat transfer between blackbodies) calculated with EMT, SiC-SiO_2 (MD) multilayer, SiO_2-SiC (DM) multilayer. The fill fraction of SiC layer is 0.4 and the unit cell size is 50nm. The gap is 200nm. Here we consider two semi-infinite slabs. One slab is at 500K and the other at 0K. There are two distinct peaks. The left and right one correspond to type II and type I hyperbolic regions, respectively. The higher peaks in the MD curve are due to the surface phonon polaritons of the topmost metallic layers. (b) Wavevector resolved heat transfer of SiC-SiO_2 (MD) multilayer normalized to blackbody limit, the three red bright regions clearly show the origin of the three peaks in (a) and the high-k states in hyperbolic regions.

2.6.5 Near field heat transfer

Now we utilize Eq. (2.46) in the heat transfer section to examine heat transfer between two plates composed of identical HMMs. Fig. 2.9(a) shows the heat transfer spectrum normalized to blackbody between two HMMs separated by a vacuum gap of 200nm. It is seen that only in regions of hyperbolic behavior we see super-Planckian thermal energy transfer in agreement with our previous analytical approximation of thermal topological transitions in near-field energy density. We note that the surface states at the interface of the topmost layer and vacuum plays a significant role in energy transfer when the top layer is metallic (Fig. 2.9(a)). This is similar to case of near-field imaging where surface plasmon polaritons at both the object plane and image plane contribute significantly to resolution enhancement; a phenomenon not captured in EMT descriptions. In Fig. 2.9(b), we show the wavevector resolved heat transfer for a multilayer metamaterial which clearly elucidates the role of high-k metamaterial states in the heat transfer.

2.7 Conclusion

This work shows that extension of equilibrium and non-equilibrium fluctuational electrodynamics to the case of metamaterials can lead to novel phenomena and applications in thermal photonics. We presented a unified picture of far-field and near-field spectra for experimentalists and also introduced the near-field spatial coherence properties of hyperbolic metamaterials. We have analyzed in detail thermal topological transitions and super-Planckian thermal emission and heat transfer in practical phonon-polaritonic hyperbolic metamaterials. We paid particular attention not only to the effective medium approximation but discussed all non-idealities limiting the super-Planckian thermal emission from HMMs. We have provided practical designs to experimentally measure and isolate our predicted effect. Our work should lead to a class of thermal engineering applications of metamaterials.

Chapter 3

Singular evanescent wave resonance

3.1 Introduction

In the previous chapter, we have examined the photon transfer and the energy associated with them between two plates at different temperatures. Another property photons possess is momentum. However, for two stationary plates, due to the symmetry of the structure, a photon with frequency and momentum $(\omega, \vec{k})$ will be emitted/absorbed at identical probability with photon $(\omega, -\vec{k})$, and thus no net momentum transfer can occur. But if we consider an asymmetric setup where one plate, say plate 2, is moving at a constant velocity V parallel to its interface (along x direction), photons with opposite momentums will be scattered at different rate due to the Doppler shift caused by the relative motion. The frequency and wavevector perceived by the moving plate are Doppler shifted and thus different from those perceived by the stationary plate. Photons with positive momentum, propagating along the moving direction, will be shifted to lower frequencies, while those with negative momentum, propagating against the moving direction, will be shifted to higher frequencies. This asymmetry leads to differences in the Bose-Einstein occupation number and the scattering matrix for $(\omega, \vec{k})$ and $(\omega, -\vec{k})$ photons, thereby causing a net momentum transfer between the moving plates even at the same temperature. Actually the momentum transfer between moving plates is an example of the research field on 'dynamical Casimir forces' that focuses on fluctuational forces between moving objects [112–114], and can be solved by combining Lifshitz's

theory [6] and electrodynamics in moving media [96]. But here we will stick to the simple photon exchange picture (see Eq. 2.47-2.51), and directly give the final result for the force which has clear physical interpretation. The lateral force between the moving plates is the product of photon exchanged and the momentum of each photon ($\hbar k_x$),

$$\begin{aligned} F(d,T_1,T_2) &= \int_0^\infty \frac{d\omega}{2\pi}\hbar k_x(n(\omega,T_1)-n(\omega',T_2)) \\ &= \sum_{j=s,p}\left\{\int_0^{k_0}\frac{d^2k_\parallel}{4\pi^2}\frac{(1-\left|r_j^{01}\right|^2)(1-\left|r_{j,mov}^{02}\right|^2)}{\left|1-r_j^{01}r_{j,mov}^{02}e^{2ik_zd}\right|^2}\right. \\ &\left.+\int_{k_0}^\infty\frac{d^2k_\parallel}{4\pi^2}e^{-2\,\mathrm{Im}(k_z)z}\frac{4\,\mathrm{Im}(r_j^{01})\,\mathrm{Im}(r_{j,mov}^{02})}{\left|1-r_j^{01}r_{j,mov}^{02}e^{2ik_zd}\right|^2}\right\}. \end{aligned} \tag{3.1}$$

Here, $r_{j,mov}^{02}$ denotes the reflection from the moving plate 2. The frequency shift from ω to $\omega' = \omega - k_x V$ in $n(\omega', T_2)$ is necessary and important because the occupation number should be counted in the plate's rest frame.

Interestingly, we find that the denominator $\left|1-r_j^{01}r_{j,mov}^{02}e^{2ik_zd}\right|$ in the above expression can be exact zero for the moving plates, which can never occur in the stationary case. This vanishing multi-reflection factor means a singular Fabry-Perot resonance with infinite quality factor, while any conventional resonance in passive, stationary system should have finite quality fact because of causality. The singular resonance leads to divergent dissipative force between the moving plates. We next start from the conventional Fabry-Perot resonance and demonstrate how the moving system can support a singular resonance and why the force diverges step by step.

3.2 Fabry-Perot resonance

The canonical example of a resonator is the Fabry-Perot (FP) system consisting of two reflecting plates separated by a vacuum gap [5, 115]. Light bouncing between them serves as a textbook introduction to the concept of a resonance and is the basis of practical devices from the laser to the interferometer [5, 115]. A simple argument suffices to understand this resonance. The reflection coefficient of propagating waves with frequency ω from the first mirror ($r_1(\omega)$) times that of the second mirror ($r_2(\omega)$) along with the propagation phase accumulated over a round trip (e^{2ik_zd}) should reconstruct the wave, capturing

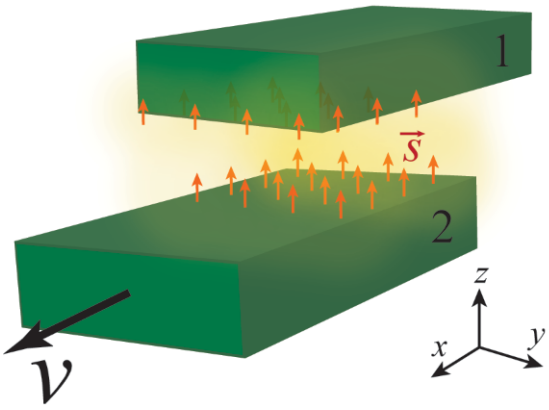

Figure 3.1: Singular Fabry-Perot (FP) resonance of evanescent waves can be achieved by setting the FP plates in relative motion. Plate 1 is stationary while plate 2 is moving at a constant velocity V along the x direction. The reflection coefficients and the distance for the moving case can lead to a perfect balance of both phase and amplitude which cannot occur for stationary plates.

it inside, leading to a resonant build-up of intensity. Here, d is the vacuum gap between the mirrors and k_z is the propagation constant perpendicular to the mirrors. We arrive at the Fabry-Perot resonance condition

$$r_1(\omega)r_2(\omega)e^{2ik_z d} = 1, \tag{3.2}$$

which also follows from a plane wave multiple scattering approach.

It is well known that this above equation cannot be fulfilled by any passive media. Note that the reflection coefficients are complex signifying the change in phase and amplitude of the propagating wave at the mirrors. A closer look reveals that an optimum choice of the gap can possibly lead to a net phase balance ($\arg(r_1(\omega)r_2(\omega)e^{2ik_z d}) = 2n\pi$) for a resonance, but material absorption and non-ideal reflections necessarily require $|r_1(\omega)r_2(\omega)| < 1$ (Fig. 3.2(a)). A gain medium is needed to compensate for this loss in amplitude as in a laser. The arguments presented above can be generalized to arbitrary passive structures showing that the bound resonances are signified by the poles of the scattering matrix which always lie in the lower half ($\mathrm{Im}(\omega_{res}) < 0$) of the complex frequency plane [116]. This condition ensures that all resonances decay in time leading to a finite quality factor.

In this work, we show that the conventional Fabry-Perot condition has fundamental differences in the case of moving media. We explain that evanescent

waves bouncing between moving plates can lead to a resonance with perfect amplitude and phase balance. We consider cases in which such a resonance, which necessarily requires negative frequency modes, can be excited in a practical scenario. Finally, we show that non-equilibrium processes (momentum and heat transfer) would be dominated by this resonance making our predicted effect viable for experimental verification. We emphasize at the outset that our result is valid taking into account polarization mixing that occur in photonic interactions between moving bodies and we predict unique scaling laws in frictional force arising due to the predicted resonance which have not been elucidated till date.

3.3 Perfect phase and amplitude balance

The case for evanescent waves in a Fabry-Perot configuration is interestingly different. They do not have phase propagation and the amplitude of such waves exponentially decays within the vacuum gap. However, those evanescent waves which couple to the surface modes of the mirror can have a reflection coefficient with amplitude greater than unity (Fig. 3.2(b)). Such waves can thus have $|r_1(\omega)r_2(\omega)| > 1$ to compensate the evanescent decay within the gap as well as non-ideal mirror reflections. The important condition of phase balance however always remains unfulfilled. This is because the mirrors necessarily impart a phase change to the evanescent waves which cannot be compensated while propagating. We also note that the mirrors can never balance or cancel the phase imparted to the evanescent wave by each other irrespective of their dielectric properties. This can be discerned by relating the phase of reflection to the energy which always tunnels into a passive medium. The energy of incident evanescent waves on any medium is given by the normal component of the Poynting vector (see Appendix A)

$$S_z = \frac{1}{2}\,\mathrm{Re}(E \times H^*)_z = \frac{|k_z|}{2\omega\mu_0} 2\,\mathrm{Im}(r). \tag{3.3}$$

For passive media, the energy tunneling into the medium is positive ($S_z > 0$, $\mathrm{Im}(r) > 0$) implying that the complex reflection coefficient of evanescent waves lies in the upper half of the complex plane and $0 < \arg(r(\omega)) < \pi$. Thus the product of the reflection coefficients at the two mirrors can never be purely real ($0 < \arg(r_1(\omega)r_2(\omega)) < 2\pi$) for evanescent waves as required for the resonance

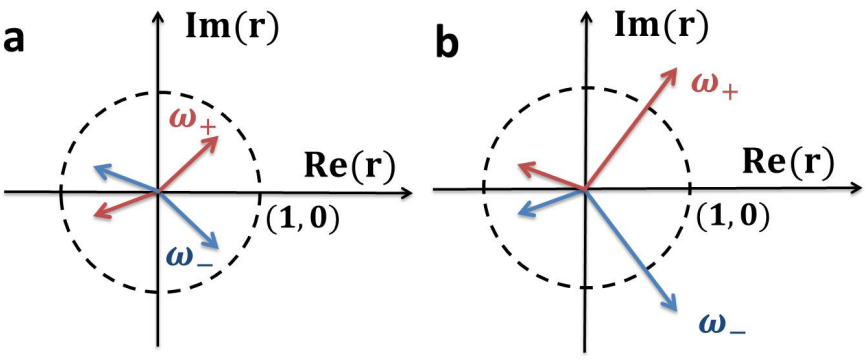

Figure 3.2: Complex reflection coefficients in passive media for positive (red) and negative frequencies (blue) (a) For propagating waves, the magnitude of the reflection coefficient should be smaller than one but there is no restriction on the phase. (b) For evanescent waves incident on a medium, the direction of energy tunneling is fixed ($S_z \propto \mathrm{Im}(r) > 0$) implying that r should be in the upper complex space (both red phasors in the figure lie in the upper half of the complex plane). The magnitude $|r|$ can be larger than one especially at surface wave resonances. We also illustrate the reflection coefficients for negative frequency propagating and evanescent waves which are complex conjugates of their positive frequency counterpart (blue phasors). Note that for evanescent waves, $r(\omega)r(-\omega)$ can be a real number larger than one leading to the possibility of a singular resonance condition (Eq. 3.2).

in Eq. (3.2). Therefore we suggest an additional condition

$$r_2(\omega) = r_1^*(\omega) \tag{3.4}$$

which fulfills the phase balance condition for evanescent waves at the mirrors. This leads to the Fabry-Perot resonance condition for evanescent waves $r_1(\omega)r_1^*(\omega)e^{-2\,\mathrm{Im}\,k_z d} = 1$. We emphasize that phase balance occurs since the phase $\arg(r_1(\omega)r_1^*(\omega)e^{-2\,\mathrm{Im}\,k_z d}) = 0$. Simultaneously amplitude balance arises since the L.H.S of Eq. (3.2) $|r_1(\omega)r_1^*(\omega)e^{-2\,\mathrm{Im}\,k_z d}| = |r_1(\omega)|^2 e^{-2\,\mathrm{Im}\,k_z d}$ can actually be unity when the exponential decay ($e^{-2\,\mathrm{Im}\,k_z d}$) is compensated by the enhancement ($|r(\omega)| > 1$) due to evanescent coupling with surface waves.

The complex conjugation of the reflection coefficient ($r^*(\omega)$) for evanescent wave Fabry-Perot resonances can be obtained by considering the negative frequency counterpart ($r(-\omega)$) since the reality of fields [116] requires $r(-\omega) = r^*(\omega)$. Thus the problem of achieving such a resonance reduces to transforming the reflection from the second mirror into the negative frequency reflection coefficient of the first mirror $r_2(\omega) = r_1(-\omega)$. This can be achieved

by setting two plates made of the same material in relative motion but with a fixed gap between them (Fig. 3.1)).

We now analyze the resonant modes within this gap. Consider an incident plane wave in vacuum given by $e^{i(\vec{k}\cdot\vec{r}-\omega t)}$ on a moving interface. We consider the lateral wavevector (k_x, k_y) along the non-relativistic moving direction ($V/c \ll 1$ and $k_y = 0$) and provide the generalized approach in Appendix A. The frequency of the wave in the frame co-moving at a constant velocity V along the x axis is Doppler shifted to $\omega' = \omega - k_x V$ [5]. This shifted frequency appears negative ($\omega' = \omega - k_x V < 0$) to the second plate for waves with $k_x > \omega/V$. Such waves have large wavevectors lying beyond the light line ($k_x \gg \omega/c$) and are necessarily evanescent in the gap.

We conclude that an evanescent wave with frequency ω incident on the stationary plate 1 will appear Doppler shifted to $-\omega$ for the moving plate 2 when $-\omega = \omega - k_x V$. We call this the phase balance wavevector,

$$k_x^{PB} = 2\frac{\omega}{V} \tag{3.5}$$

Evanescent waves with this special wavevector will bounce off the stationary first mirror with reflection coefficient $r_1(\omega)$ but reflect off the second identical but moving mirror with coefficient $r_2^{mov}(\omega) = r_1(-\omega) = r_1^*(\omega)$ (see Appendix A).

We emphasize now the fundamental difference between the stationary plate [117] and moving plate cases. Using the near-field quasi-static approximation, the stationary plates would lead to the well-known condition found in text-books,

$$r_p^2 e^{-4\omega d/V} = 1 \tag{3.6}$$

where r_p is the reflection coefficient of p-polarized waves. As explained previously, the complex nature of the reflection coefficient implies this condition cannot be fulfilled irrespective of distance or material properties. This result has been utilized extensively in laser physics and also extended to the case of Casimir force [117]. Our aim here is to show that subtle balance of phase and amplitude are completely missed by the above equation. The moving plate case gives rise to a counterintuitive singular resonance condition

$$|r_p|^2 e^{-4\omega d/V} = 1 \tag{3.7}$$

The subtle role of the negative frequency mode is revealed in the phase cancellation on reflection which cannot occur for stationary plates. We note now that there is a critical distance which can lead to a singular resonance condition

$$d^{AB} = \frac{V}{2\omega} \ln |r_p(\omega)| \,, \tag{3.8}$$

The central result in our work is the combination of Equations (3.5), (3.7) and (3.8) and the invalidity of (3.6) for the moving case even though it is widely used. Note we require $|r_p| > 1$ which can occur if the plate supports surface waves. The phase balance (PB) (Eq. (3.5)) and amplitude balance (AB) condition (Eq. (3.7)) together can achieve the singular Fabry-Perot condition for evanescent waves bouncing between moving media.

We emphasize that this condition holds true in the relativistic case as well leading to a singular resonant condition in spite of the presence of material dispersion and absorption. A detailed proof of this result taking into account polarization mixing is given in the Appendix A. We note that a complete numerical calculation taking into account polarization mixing produces all the scaling laws mentioned in the subsequent sections. Furthermore, the relativistic phase balance wavevector $k_x^{PB} = (1 + 1/\gamma)\omega/V$ also makes the relativistic multi-reflection which includes polarization mixing to be completely real. We show in Appendix A information that one can always find a distance that makes this real multi-reflection factor exactly zero.

3.4 Excitation of the perfect resonance

Coupling energy from the far-field into near-field to excite the singular resonant mode becomes increasingly inefficient as the spectral width of the mode decreases. However, we show that evanescent wave Fabry-Perot modes with vanishing spectral width can be thermally excited between moving bodies without the need for any external optical excitation. Near-field plates at different temperatures exchange thermal energy through excitation of allowed evanescent gap modes [17, 29]. However, even if we consider the temperature T of the identical plates to be the same, the Bose-Einstein distribution [2] of thermally excited modes $n(\omega, T) = 1/(e^{\hbar\omega/k_B T} - 1)$ within the moving plate will be Doppler shifted from the stationary plate. This drives an interesting photon exchange between the plates through the singular resonance. The oc-

cupation of modes in the moving plate, which have to be evaluated in the co-moving frame, will be negative specifically for those modes which have negative Doppler shifted frequencies, since the Bose-Einstein distribution gives $n(\omega', T_2) = -1 - n(-\omega', T_2)$ for $\omega' < 0$ [118]. We emphasize that this negative occupation is indicative of an excitation akin to population inversion made possible by the energy of motion.

The photon exchange between the plates is also governed by the emissivity or absorptivity of the plates in the near-field [17, 22, 38, 104]. The near-field emissivity of a plate is proportional to the evanescent wave Poynting vector ($S_z \propto \mathrm{Im}(r(\omega))$). There is a stark contrast between the Poynting vector directions for positive frequencies and negative frequencies (evanescent waves with $k_x > \omega/V$). Since $r(-\omega) = r^*(\omega)$, we see that the Poynting vector of tunneling negative frequency waves $S_z \propto \mathrm{Im}(r)$is opposite to that of positive frequency waves. Therefore the emissivity of the moving plate is negative while that of the stationary plate is positive for negative frequency modes. We thus note that as opposed to the conventional case of light tunneling into a medium, the negative frequency evanescent modes supported by a moving medium can tunnel out of it (Fig. 3.1). These photons will subsequently be absorbed by the stationary plate. The net photon emission rates for the two plates are positive and given by $N_1 = 2\,\mathrm{Im}(r_1(\omega))n\,(\omega, T_1)$ and $N_2 = 2\,\mathrm{Im}(r_2^{mov}(\omega))n\,(\omega', T_2)$ respectively. By generalizing Kirchoff's law to the near-field, we see that the near-field absorptivity of the plates is also given by $2\,\mathrm{Im}[r(\omega)]$. Thus the number of photons emitted by the stationary plate and then absorbed by the moving plate is $N_{1\to2} = N_1 2\,\mathrm{Im}\,[r_2^{mov}(\omega)]$, which is negative due to the negative absorptivity of the moving plate. This negative absorptivity implies the moving plate, which is in an excited state, is losing photons instead of absorbing them. It is the excitations from the stationary plate which cause the stimulated emission of photons from the moving plate. Similarly, the number of photons emitted by the moving plate and then absorbed by the stationary plate is $N_{2\to1} = N_2 2\,\mathrm{Im}\,[r_1(\omega)]$ which is positive as expected.

The evanescent photons exchanged between the plates $N = N_{2\to1} - N_{1\to2}$ is [38]

$$N(\omega, k_x) = \frac{2\,\mathrm{Im}\,[r_1(\omega)]\left|e^{ik_z d}\right|^2 2\,\mathrm{Im}\,[r_2^{mov}(\omega)]\,(n(\omega', T_2) - n(\omega, T_1))}{\left|1 - r_1(\omega) r_2^{mov}(\omega) e^{2ik_z d}\right|^2}, \tag{3.9}$$

where $r_1(\omega)$ and $r_2^{mov}(\omega)$ are the reflection coefficients for the stationary and

moving plates respectively evaluated for a wave incident with frequency ω in the lab frame. We have $r_2^{mov}(\omega) = r_1(\omega')$ and the factor $\left|e^{ik_{zd}}\right|^2$ accounts for the decay of the photon propagating between the two plates while the denominator $\left|1 - r_1(\omega) r_2^{mov}(\omega) e^{2ik_z d}\right|^2$ is for the multi-reflection between the plates. Firstly, we note that at zero temperature, if $\omega' < 0 < \omega$, we have $n(\omega', 0) = -1$ and $n(\omega, 0) = 0$, so the difference $n(\omega') - n(\omega, 0)$ is nonzero; thus photon exchange occurs even at zero temperature, which causes quantum friction. Secondly, even though the multi-reflection factors are routinely encountered in the case of parallel plates, once they are set in motion we predict a critical difference. For frequencies at which the plates support surface waves, the singular Fabry-Perot resonance of evanescent waves can lead to the divergence of this multi-reflection factor for the phase balance wavevector ($k_x^{PB} = 2\omega/V$) and amplitude balance distance ($d^{AB} = (V/2\omega) \ln |r_p(\omega)|$). The role of evanescent waves and surface waves in the mediation of energy transfer as well as Casimir forces are well known [29, 117]. However, the presence of surface waves does not in any way imply the delicate phase and amplitude balance condition described above.

To analyze the nature of the excited evanescent wave resonance in a practical scenario, we consider two identical metallic plates moving relative to each other at non-relativistic speeds. The moving velocity is bounded by the phonon velocity of the medium [89], typically in the order of 10^4m/s, thus $\beta = V/c \ll 1$. The plates are separated by a small gap to allow for interaction through large wavevector evanescent waves, necessary to achieve Doppler shifted negative frequencies in the co-moving frame. Since phase balance wavevector k_x^{PB} $(2k_0/\beta)$ is much larger than k_0, the reflection coefficient for p-polarized waves can be approximated by $r_p(\omega) = (\epsilon(\omega) - 1)/(\epsilon(\omega) + 1)$. When $\mathrm{Re}(\epsilon(\omega)) = -1$, there occurs a pole of the reflection coefficient corresponding to the surface wave resonance (SWR). The amplitude enhancement of an evanescent wave has a maximum at this SWR ω_{SWR}, leading to the critical distance $d_0 = V/(2\omega_{SWR}) \ln |r_p(\omega_{SWR})|$. At the SWR frequency, the magnitude of reflection coefficient $|r_p|$ is bounded by the loss of the material. Realistic estimates for $|r_p|$ is in the order of 10 and if the plate velocity is 10^4m/s, the operating frequency ω_{SWR} should be in the order of 10^{12}Hz to give a critical distance in the order of 10 nm. Thus we need materials with low plasma frequency in the THz region to observe the singular Fabry-Perot resonance of evanescent waves. Here we consider a Drude metal with frequency dependent permittivity given by $\epsilon(\omega) = 1 - \omega_p^2/(\omega^2 + i\Gamma\omega)$ with $\omega_p = 3 \times 10^{12}$Hz

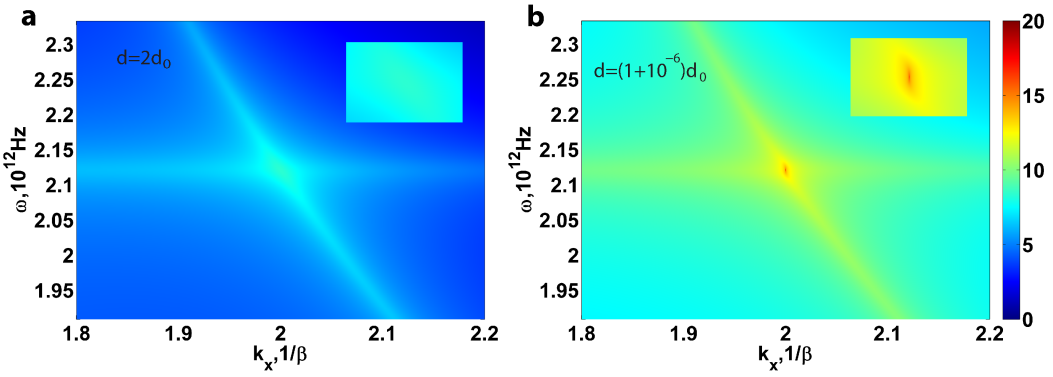

Figure 3.3: Contribution to exchanged photon number resolved by frequency and lateral wavevector k_x (normalized to free space wavevector) at (a) $d = 2d_0$ and (b) $d \to d_0^+$ ($d = (1 + 10^{-6})d_0$). In both (a) and (b), we see two bright curves, both of which are due to surface wave resonances. In (a), at a distance away from d_0, the singular resonance condition is far from being satisfied. However, the bright curves remain due to the SWR at the two interfaces. In (b), the red bright point is due to the singular resonance that arises since the amplitude balance condition is satisfied when $d \to d_0^+$ and phase balance condition is satisfied at $k_x = 2/\beta$. This leads to giant photon exchange between moving plates at the singular resonance. The insets give the zoom in plots near the intersection of the two SWRs. See also Fig. A.7.

and $\Gamma = 0.01\omega_p$. The temperatures are chosen to be T_1=320K and T_2=300K. The SWR frequency for this material is 2.12×10^{12}Hz and at the velocity of 10^4m/s, the critical distance d_0 that satisfies the singular resonance condition is close to 10nm.

In Fig. 3.3, we plot the spectrum of photons exchanged according to their frequency and wavevector in the lab frame. For a distance d_1 which is away from the singular Fabry-Perot Resonance condition, we see two distinct bright regions in $\omega - k$ space through which photons are exchanged between the two plates. The horizontal region corresponds to the SWR frequency of the stationary plate where all wavevectors are excited like in a conventional surface wave resonance [103]. The curved region corresponds to the Doppler shifted SWR frequency of the moving plate. We emphasize that previous work on quantum friction [21, 38, 89–102] has been limited to these modes and the corresponding scaling laws.

Our result shows that as the plates are moved closer to the singular FP resonance condition ($d \to d_0^+$), a fundamentally new mechanism of photon exchange emerges. This is evident from Fig. 3.3(b) where photons with the

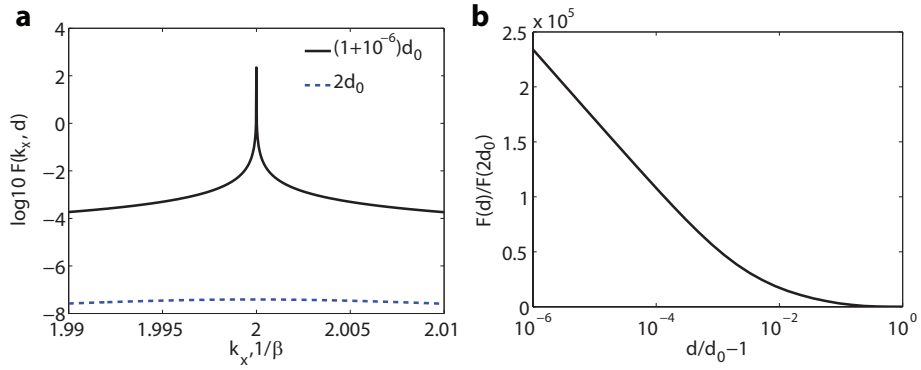

Figure 3.4: Non-equilibrium vacuum friction on the FP plates (a) resolved by the wavevector k_x at $d = d_0^+$ and $d = 2d_0$. A major contribution to the force arises from modes at the perfect phase balance wavevector. Note, at $2d_0$, the amplitude of friction is significantly smaller. (b) The distance dependence of friction at distances near d_0. The x axis is in $(d/d_0 - 1)$ and log scale. We clearly see a linear increasing behavior as d approaches d_0. This is consistent with the theoretical scaling law which predicts a logarithmic divergence of the non-equilibrium vacuum friction in the ideal limit.

phase balance wavevector completely dominate the interaction. Note that this occurs when the frequencies in the co-moving frame and lab frame are equal and opposite, the condition for phase balance. Indeed, the multiple scattering term $1-r_1r_2e^{2ik_zd}$ in Eq. (3.9), vanishes giving rise to an infinitely large number of photons exchanged.

3.5 Giant dispersive force between the plates in relative motion

We assert that the singular evanescent wave resonance fundamentally dominates all non-equilibrium processes between the plates. We focus here on the observable force on the plates in a direction opposite to the motion, which arises due to momentum carried by the photons exchanged between the plates. This dispersive force, i.e., the momentum transfer between the two plates[11], is the product of the total number of photons exchanged (Eq. 3.9) and the momentum of a single photon $\hbar k_x$ giving $f_x(\omega, k_x) = \hbar k_x N(\omega, k_x)$ where the net force $F = \int f_x(\omega, k_x) dk_x$.

In Fig. 3.4(a), we plot the spectrum of this non-equilibrium vacuum friction force resolved according to the wavevector for various distances of the

plates. The largest contribution to the force is due to the singular Fabry-Perot resonance of evanescent waves. This can be interpreted as a perfect coupling of positive and negative frequencies in the near-field.

When the distance d approaches the critical distance d_0, we predict the non-equilibrium friction F to be

$$F \sim \ln\left(\frac{d_0}{d-d_0}\right) \tag{3.10}$$

This result holds true for the quantum friction (T→0) case as well. We plot the friction vs. distance in Fig. 3.4(b) to verify the theoretical predictions. We clearly see that the friction increases as $\ln[d_0/(d-d_0)]$ when d approaches d_0. In fact, it is interesting to note that this singular resonance causes the frictional force to actually diverge under the macroscopic electrodynamic assumption [1] used routinely. This is fundamentally different from previous works [21,38,89–102] that have calculated forces and scaling laws. The reason for the difference is that previous works did not consider the effect of the unique resonance and critical distance.

In Fig. 3.4(b), the magnitudes of friction evaluated around the resonance at $d_1 = 2d_0$ and $d_2 = (1+10^{-6})d_0$ are $4.58 \times 10^{-5}\mathrm{N/m^2}$ and $10.7\ \mathrm{N/m^2}$, respectively. We do not assume ideal mirrors [119] and losses or dispersion are not an impediment to the singular resonance. Our estimates are based on assumptions of a local Drude model which will be modified for electromagnetic interactions with large wavevectors [120, 121]. However, the only fundamental requirement is the enhancement in the reflection of coefficient of evanescent waves which is known to occur even in the presence of non-locality (eg: graphene plasmons [122,123]). This giant enhancement in non-equilibrium momentum and heat transfer due to the resonance predicted in this work can be ascertained either with THz surface waves in degenerately doped semiconductors [73], phonon-polaritonic polar dielectrics [124], low frequency plasmons or graphene [125]. The role of the giant photon flux caused by the resonance on assumptions of macroscopic and local fluctuational electrodynamics will be analyzed in future work. Our results can be extended to the case of energy transfer as well where we expect a giant exchange in energy between the plates due to the singular resonance condition.

3.6 Conclusion

In essence, the singular resonance occurs when the pole of a scattering matrix is pulled up to the real axis due to the relative motion of the plates [126]. We note that this is precluded by the requirement of an infinite energy supply for maintaining relative motion near this resonance condition. We emphasize that the singular resonance we introduced can be adopted to plates at any temperatures including the low temperature limit of quantum friction. Our result is fundamentally related to classical electromagnetic scattering theory and is unrelated to the debate on quantum friction ($T \to 0$ case). Furthermore, there is a consensus in the literature about the non-equilibrium vacuum friction case which we have chosen to elucidate [118, 127].

In summary, we have introduced a singular resonance supported by moving media caused by the perfect coupling of positive and negative frequencies in the near-field. Experiments with light induced potentials [128] or nanomechanical [129] systems can manifest such resonances leading to a deeper understanding of negative frequency modes [130, 131].

Chapter 4

Conclusion

We have fully developed fluctuational electrodynamics in multi-layered structures at equilibrium or non-equilibrium. Both first principle second kind of fluctuation dissipation theorem and the scattering matrix formalism are employed and confirmed to be equivalent. With dyadic Green's function in multi-layered structures, we are able to calculate the energy density, Poynting vector, spatial coherence of the electromagnetic fields in such structures. We have limited ourselves to multi-layered structures which have simple analytic dyadic Green's functions. For complex geometries where no such analytic DGFs are available, one should use numerical methods such as finite element method, finite-difference time-domain and boundary element method [46, 47, 110, 111], which will be studied in future work.

We have applied the theory to examine thermal properties of practical hyperbolic metamaterials composed of multilayer phonon-polaritonic materials. The high wavevector states in hyperbolic metamaterials lead to near field thermal emission and heat transfer that exceed the black body limit in a broad bandwidth. Furthermore, the high wavevector states have a large impact on the spatial coherence of the thermal fields. We have utilized both effective medium theory and transfer matrix method to compute the scattering matrix of the multi-layered structures and shown the regions where effective medium theory is valid. Our results could be verified in experiments and potentially applied in energy harvesting industry, especially in enhancing the efficiency of solar cells.

We have also introduced a singular Fabry-Perot resonance of evanescent waves bouncing between two plates at relative motion. The resonance arises due to the coupling of positive and negative frequency evanescent waves and

leads to a spontaneous exchange of a large number of photons between the moving bodies. The non-contact frictional force mediated by a nanoscale vacuum gap can diverge due to the existence of this singular evanescent wave Fabry-Perot resonance. Thus essentially an infinite force is required to keep the plate at the constant velocity, complying with causality.

We have shown the singular resonance leads to divergent dispersive force between the two plates in spite of loss of the material, polarization mixing as well as relativistic effects. However, non-local effects occur due to the large wavevector and the close spacing between the plates [132]. Moreover, as the energy exchange between the two plates goes up, the large field intensity will cause nonlinear effects. In the theory part, we have essentially assumed the validity of linear scattering process. The fluctuational electrodynamics theory in Ref. [96] is based on linear response theory [133]. The nonlinear response of the media will certainly play an important role near the singular resonance. Thus we argue that non-locality and nonlinear effects might curtail the singularity, especially due to breakdown of linear response theory near the singular resonance. The role of non-locality and nonlinear effects will be examined in future work.

Appendix A

Supplementary information for singular evanescent wave resonance

A.1 Derivation of Poynting vector

A p-polarized incident plane wave,$H_i = \hat{y}e^{i(k_x x+k_y y+k_z z-\omega t)}$, shines on the interface in x-y plane between vacuum and a plate. Here k_x and k_y are real, $k_z = \sqrt{(\omega/c)^2 - k_x^2 - k_y^2}$, k_z is real for propagating waves (PWs) while imaginary for evanescent waves (EWs). Assuming that the reflection coefficient is r, the reflected wave will be $H_r = \hat{y}re^{i(k_x x+k_y y-k_z z-\omega t)}$. The electric fields lying along the interface are $E_{ix} = \hat{x}\frac{k_z}{\omega\mu_0}e^{i(k_x x+k_y y+k_z z-\omega t)}$, $E_{rx} = \hat{x}\frac{-k_z r}{\omega\mu_0}e^{i(k_x x+k_y y+k_z z-\omega t)}$. Thus the Poynting vector [5] along the normal direction is

$$S_z = \frac{1}{2}\,\mathrm{Re}(E \times H^*)_z = \begin{cases} I\frac{|k_z|}{\omega}(1-|r|^2), \mathrm{PWs} \\ \\ I\frac{|k_z|}{\omega}2\,\mathrm{Im}(r), \mathrm{EWs} \end{cases}, \tag{A.1}$$

where I is a constant proportional to the intensity of the incident waves. Then the energy absorbed by the plate is proportional to $1-|r|^2$ for PWs and $2\,\mathrm{Im}(r)$ for EWs. For a stationary passive medium, S_z must be positive so $1-|r|^2 > 0$ for PWs and $\mathrm{Im}(r) > 0$ for EWs. It is worthwhile noting that $1-|r|^2$ is the far field emissivity related to the absorption of propagating waves and $2\,\mathrm{Im}(r)$ can be physically interpreted as the near field emissivity [22, 38, 104] in the photon emission process. The above result has been utilized throughout the

manuscript to understand the tunneling of evanescent waves emanating from the moving mirror.

A.2 On the reality of fields

The key condition for the Fabry-Perot resonance of evanescent waves is obtained by the complex conjugation of the reflection coefficients. In the main text we have argued that this can be achieved using the negative frequency counterpart of the reflection coefficient. This result relies on the condition for the reality of the fields [116]. In Fourier space, the electric fields are expressed as

$$E(r,t) = \int u(\omega, k_x, k_y, z) e^{i(k_x x + k_y y - \omega t)} dk_x dk_y d\omega. \tag{A.2}$$

In view of the reality of $E(r,t)$,

$$u(\omega, k_x, k_y, z) = u^*(-\omega, -k_x, -k_y, z). \tag{A.3}$$

This is valid for both the incident waves and the reflected waves. For reflections from a stationary plate with the in plane wavevectors (k_x, k_y) conserved,

$$r(\omega, k_x, k_y) = r^*(-\omega, -k_x, -k_y). \tag{A.4}$$

In this work, we assume the reflection coefficients are written for isotropic media so that

$$r(\omega, k_x, k_y) = r(\omega, -k_x, -k_y). \tag{A.5}$$

Thus for reflection from a stationary plate, we have

$$r(\omega, k_x, k_y) = r^*(-\omega, k_x, k_y). \tag{A.6}$$

A.3 The scattering matrix of a moving plate with polarization mixing

In the main text, for simplicity, we have assumed non-relativistic velocities and no mixing of polarizations. However, here we generalize our approach and show that the central result related to the singular resonance of evanescent waves persists even in the relativistic limit.

We start from the Lorentz transformation [5],

$$\begin{bmatrix} E' \\ cB' \end{bmatrix} = \gamma \begin{bmatrix} \overleftrightarrow{\alpha}^{-1} & \overleftrightarrow{\beta} \\ -\overleftrightarrow{\beta} & \overleftrightarrow{\alpha}^{-1} \end{bmatrix} \begin{bmatrix} E \\ cB \end{bmatrix}, \tag{A.7}$$

where

$$\overleftrightarrow{\alpha}^{-1} = \begin{bmatrix} 1/\gamma & 0 & 0 \\ 0 & 1 & 0 \\ 0 & 0 & 1 \end{bmatrix}, \overleftrightarrow{\beta} = \begin{bmatrix} 0 & 0 & 0 \\ 0 & 0 & -\beta \\ 0 & \beta & 0 \end{bmatrix}, \tag{A.8}$$

with $\beta = V/c$, $\gamma = 1\Big/\sqrt{1-\beta^2}$.

The electric fields are transformed by

$$E' = \gamma(\overleftrightarrow{\alpha}^{-1} E + \overleftrightarrow{\beta}\, cB). \tag{A.9}$$

For plane waves with phase $e^{i(k_x x + k_y y + k_z z - \omega t)}$,

$$cB = \frac{c}{\omega}\vec{k} \times E = \frac{c}{\omega} \begin{bmatrix} 0 & -k_z & k_y \\ k_z & 0 & -k_x \\ -k_y & k_x & 0 \end{bmatrix} E = \frac{c}{\omega} \overleftrightarrow{k}\, E. \tag{A.10}$$

For the frequency and wavevector, the Lorentz transformation gives [5],

$$k_x^{'} = \gamma(k_x - \beta k_0), \tag{A.11}$$

$$\omega' = \gamma(\omega - k_x V), \tag{A.12}$$

while k_y and k_z remain unchanged. Note that under non-relativistic limit, we have $k_x^{'} = k_x$ and $\omega' = \omega - k_x V$ which are used in the main text.

We first transform the incident field to the co-moving frame,

$$E' = \gamma(\overleftrightarrow{\alpha}^{-1} + \frac{c}{\omega}\overleftrightarrow{\beta}\overleftrightarrow{k})E. \tag{A.13}$$

The reflected fields in the co-moving frame are

$$E_r^{'} = (r_s^{'}\hat{s}_-^{'}\hat{s}_+^{'} + r_p^{'}\hat{p}_-^{'}\hat{p}_+^{'})E'. \tag{A.14}$$

Here $\hat{s}_+^{'} = \hat{s}_-^{'} = (k_y^{'}, -k_x^{'}, 0)/k_\rho^{'}$ are the unit vectors of upward and downward s-

polarized waves, $\hat{p}^{'}_{+} = (-k^{'}_{x}k^{'}_{z}, -k^{'}_{y}k^{'}_{z}, (k^{'}_{\rho})^2)/(k^{'}_{0}k^{'}_{\rho})$, $\hat{p}^{'}_{-} = (k^{'}_{x}k^{'}_{z}, k^{'}_{y}k^{'}_{z}, (k^{'}_{\rho})^2)/(k^{'}_{0}k^{'}_{\rho})$, are the unit vectors of forward and downward p-polarized waves, respectively, where $k^{'}_{0} = \omega/c$, $k^{'}_{\rho} = \sqrt{(k^{'}_{x})^2 + (k^{'}_{y})^2}$. $r^{'}_{s}$ and $r^{'}_{p}$ are the standard Fresnel reflection coefficient of s- and p-polarized waves in the co-moving frame, respectively.

Next we transform the reflected field to the lab frame,

$$E_r = \gamma(\overleftrightarrow{\alpha}^{-1} + \frac{c}{\omega'}\overleftrightarrow{\beta}'\overleftrightarrow{k}')E'_r. \tag{A.15}$$

Here

$$\overleftrightarrow{\beta}' = \begin{bmatrix} 0 & 0 & 0 \\ 0 & 0 & \beta \\ 0 & -\beta & 0 \end{bmatrix} = -\overleftrightarrow{\beta}, \quad \overleftrightarrow{k}' = \frac{c}{\omega'}\begin{bmatrix} 0 & -k^{'}_{z} & k^{'}_{y} \\ k^{'}_{z} & 0 & -k^{'}_{x} \\ -k^{'}_{y} & k^{'}_{x} & 0 \end{bmatrix}. \tag{A.16}$$

Thus $E_r = RE$ where the reflection operator is given by

$$R = \gamma(\overleftrightarrow{\alpha}^{-1} + \frac{c}{\omega'}\overleftrightarrow{\beta}'\overleftrightarrow{k}')(r^{'}_{s}\hat{s}^{'}_{-}\hat{s}^{'}_{+} + r^{'}_{p}\hat{p}^{'}_{-}\hat{p}^{'}_{+})\gamma(\overleftrightarrow{\alpha}^{-1} + \frac{c}{\omega}\overleftrightarrow{\beta}\overleftrightarrow{k}). \tag{A.17}$$

For an alternative derivation of this reflection operator, see Ref. [98].

Now the reflection operator is written in a 3 by 3 matrix. The 2 by 2 reflection matrix is defined by

$$r_{\lambda\mu} = \hat{e}^{-}_{\lambda} R \hat{e}^{+}_{\mu}, \tag{A.18}$$

where $r_{\lambda\mu}$ are the reflection coefficients for an incident wave with polarization$\mu$to be reflected as a wave with polarization λ. $\hat{e}^{\pm}_{s} = (k_y, -k_x, 0)/k_\rho$, $\hat{e}^{\pm}_{p} = (\mp k_x k_z, \mp k_y k_z, k^2_\rho)/k_0 k_\rho$ ($k_0 = \omega/c$, $k_\rho = \sqrt{k^2_x + k^2_y}$) are the unit vector of s- and p-polarized waves in the vacuum, respectively. As before, the plus sign in the superscript of $\hat{e}$ denotes forward waves (incident waves) and the minus sign for downward waves (reflected waves). After some lengthy but straightforward calculations, the scattering matrix of the moving plate $r_{\lambda\mu}$ is found to be

$$r_{\lambda\mu} = \begin{bmatrix} r_{ss} & r_{sp} \\ r_{ps} & r_{pp} \end{bmatrix} = B \begin{bmatrix} r^{'}_{s} & \\ & r^{'}_{p} \end{bmatrix} A. \tag{A.19}$$

Here the matrix elements $A_{11} = A_{22} = \gamma k^{'}_{0}(k^2_\rho - \beta k_0 k_x)\Big/ k_0 k^{'}_{\rho} k_\rho$, $A_{12} = -A_{21} = \gamma k^{'}_{0}(-\beta k_y k_z)\Big/ k_0 k^{'}_{\rho} k_\rho$, $B_{11} = B_{22} = \gamma k_0(k^2_\rho - \beta k_0 k_x)\Big/ k_0 k^{'}_{\rho} k_\rho$, $B_{12} = -B_{21} =$

$\gamma k_0(-\beta k_y k_z)\Big/ k_0 k_\rho^{'} k_\rho$. The reflection coefficients are

$$r_{ss} = r_s^{'}\gamma^2(k_\rho^2 - \beta k_0 k_x)^2\Big/(k_\rho^{'}k_\rho)^2 - r_p^{'}\gamma^2(\beta k_y k_z)^2\Big/(k_\rho^{'}k_\rho)^2, \tag{A.20}$$

$$r_{sp} = -(r_s^{'} + r_p^{'})\gamma^2(k_\rho^2 - \beta k_0 k_x)\beta k_y k_z\Big/(k_\rho^{'}k_\rho)^2, \tag{A.21}$$

$$r_{ps} = (r_s^{'} + r_p^{'})\gamma^2(k_\rho^2 - \beta k_0 k_x)\beta k_y k_z\Big/(k_\rho^{'}k_\rho)^2 = -r_{sp}, \tag{A.22}$$

$$r_{pp} = r_p^{'}\gamma^2(k_\rho^2 - \beta k_0 k_x)^2\Big/(k_\rho^{'}k_\rho)^2 - r_s^{'}\gamma^2(\beta k_y k_z)^2\Big/(k_\rho^{'}k_\rho)^2. \tag{A.23}$$

Generally speaking, the reflected waves of p-polarized waves will have s-polarized waves component, and vice versa. This is called polarization mixing. Note polarization mixing will not be a significant effect at non-relativistic velocity due to the factor β in both r_{sp} and r_{ps}.

However, for $k_y = 0$, we have

$$r_{ss}(\omega, k_x) = r_s^{'}(\omega', k_x^{'}), \tag{A.24}$$

$$r_{pp}(\omega, k_x) = r_p^{'}(\omega', k_x^{'}), \tag{A.25}$$

and

$$r_{sp} = r_{ps} = 0. \tag{A.26}$$

This means, when $k_y = 0$, polarization mixing disappears regardless of the velocity. The reflection from a moving plate can be expressed as the standard Fresnel reflection from a stationary plate with a Doppler shifted frequency and wavevector. In the main text, we only consider the p-polarized waves with $k_y = 0$, thus $r_p(\omega, k_x) = r_p^{'}(\omega', k_x^{'})$. The polarization of the wave does not change on reflection.

At the relativistic phase balance wavevector (set $\omega' = -\omega$ in Eq. (A.12))

$$k_x = (1 + \frac{1}{\gamma})\frac{\omega}{V}, \tag{A.27}$$

we have

$$\omega' = -\omega,\ k_x^{'} = k_x. \tag{A.28}$$

Thus $r_p(\omega, k_x) = r_p^{'}(-\omega, k_x)$. Here $r_p^{'}$ is reflection from a stationary plate in the co-moving frame, so $r_p(\omega, k_x) = (r_p^{'}(\omega, k_x))^*$, which is the complex conjugate of the reflection coefficient from the stationary plate in the lab frame. In this sense, we achieve $r_2 = r_1^*$ at the phase balance wavevector.

The expression for the Poynting vector is also valid for a moving plate since it only depends on the reflection coefficients. At the lab frame, we only consider positive frequency, namely $\omega > 0$. When the Doppler shifted frequency $\omega' < 0$, $\mathrm{Im}(r)$ will be negative, resulting in a negative Poynting vector. Thus essentially we extract energy out from the moving plate.

A.4 Approximation of the reflection coefficients

The moving velocity is bounded by the phonon velocity of the medium, typically in the order of 10^4m/s, thus β is very small in the order of 10^{-4}. As k_x is very large to achieve negative frequency ($k_x > k_0/\beta$), the reflection coefficients can be evaluated by the high-k approximation. For a stationary plate with a very large k_x,

$$r_s = \frac{\epsilon - 1}{4(k_\rho/k_0)^2}, \tag{A.29}$$

and

$$r_p = \frac{\epsilon - 1}{\epsilon + 1}. \tag{A.30}$$

The reflection coefficient for s-polarized waves is negligibly small, while $|r_p|$ has a resonance at $\mathrm{Re}(\epsilon) = -1$, which is the surface wave resonance condition.

To compensate the propagating decay of evanescent waves inside the vacuum gap, $|r_p|$ should be larger than 1, thus implying $\mathrm{Re}(\epsilon) < 0$. This means the structure needs to work in the frequency spectrum where the materials are metallic.

A.5 Full theory for photon exchange

In the main text, we have argued that the spontaneously occurring photon exchange between the plates diverges due to the existence of the singular resonance condition. Here for completeness, we provide the complete relativistic theory of the photon exchange and relate it to the frictional force to emphasize how the phase balance and amplitude balance condition enters in the analysis.

In the main text, we have assumed that $k_y = 0$ to avoid polarization mixing of waves. Thus we can deal with p- and s-polarized waves separately. The scattering matrix, i.e., the reflection matrix, will be diagonal and can be handled as scalars. However, if $k_y \neq 0$, the scattering matrix $r_{\lambda\mu}$ of the moving plate will have non-diagonal terms, i.e., polarization mixing terms. Therefore we need the full theory with polarization mixing and relativistic velocity taken into account to describe the photon exchange picture.

The spontaneous emission rate from a moving plate at constant velocity is [35, 37, 38, 134]

$$\mathrm{Tr}(1 - SS^\dagger)n(\omega', T) \tag{A.31}$$

for propagating waves and

$$\mathrm{Tr}(i(S^\dagger - S))n(\omega', T) \tag{A.32}$$

for evanescent waves. Here, $S = r_{\lambda\mu}$ is the classical scattering matrix evaluated in the lab frame, ω' is the frequency in the moving plate's rest frame, $n(\omega', T)$ is the Bose-Einstein occupation number [2] in the co-moving frame, '$\dagger$' denotes Hermitian conjugate, 'Tr' means taking the trace. $(1 - SS^\dagger)$ and $i(S^\dagger - S)$ can be also seen as the absorption rate of the incident waves by the plates.

Assuming U is the spontaneous emission (absorption) amplitude of the plate [38]. For propagating waves, $UU^\dagger = 1 - SS^\dagger$; for evanescent waves, $UU^\dagger = i(S^\dagger - S)$. The amplitude of photon emitted by plate 1 and then absorbed by the plate 2 is $U_2 e^{ik_z d} U_1$, where $e^{ik_z d}$ accounts for the propagating with the vacuum gap. Taking the multi-reflection into account [4], the amplitude is

$$U_2(1 + e^{2ik_z d}S_1S_2 + (e^{2ik_z d}S_1S_2)^2 + \cdots)e^{ik_z d}U_1 = U_2\frac{e^{ik_z d}}{1 - S_1S_2e^{2ik_z d}}U_1. \tag{A.33}$$

With the Bose-Einstein occupation number $n_1(\omega, T_1)$ of plate 1, the photon transfer rate from plate 1 to plate 2 is [35, 37, 38]

$$N_{1\to2} = \mathrm{Tr}\left[(U_2\frac{e^{ik_z d}}{1 - S_1S_2e^{2ik_z d}}U_1)(U_2\frac{e^{ik_z d}}{1 - S_1S_2e^{2ik_z d}}U_1)^\dagger\right] n_1(\omega, T_1). \tag{A.34}$$

Similarly, the photon transfer rate from plate 2 to plate 1 is

$$N_{2\to1} = \mathrm{Tr}\left[(U_1\frac{e^{ik_z d}}{1 - S_2S_1e^{2ik_z d}}U_2)(U_1\frac{e^{ik_z d}}{1 - S_2S_1e^{2ik_z d}}U_2)^\dagger\right] n_2(\omega', T_2). \tag{A.35}$$

It can be shown that

$$\begin{aligned}&\mathrm{Tr}\left[(U_2\frac{e^{ik_zd}}{1-S_1S_2e^{2ik_zd}}U_1)(U_2\frac{e^{ik_zd}}{1-S_1S_2e^{2ik_zd}}U_1)^\dagger\right]\\=&\mathrm{Tr}\left[(U_1\frac{e^{ik_zd}}{1-S_2S_1e^{2ik_zd}}U_2)(U_1\frac{e^{ik_zd}}{1-S_2S_1e^{2ik_zd}}U_2)^\dagger\right].\end{aligned}\tag{A.36}$$

The net photon exchanged rate should be $N = N_{2\to1} - N_{1\to2}$. One then finds that

$$N = \mathrm{Tr}\left[(1-S_1^\dagger S_1)D(1-S_2S_2^\dagger)D^\dagger\right](n_2(\omega',T_2)-n_1(\omega,T))\tag{A.37}$$

for propagating waves, and

$$N = \mathrm{Tr}\left[(S_1-S_1^\dagger)D(S_2^\dagger-S_2)D^\dagger\right](n_2(\omega',T_2)-n_1(\omega,T))\tag{A.38}$$

for evanescent waves, where $D = e^{ik_zd}/(1-S_2S_1e^{2ik_zd})$.

With the help of the scattering matrix and after some algebra, one can derive the expression for number of photon exchanged,

$$\begin{aligned}&N(\omega,k_x,k_y) = (n(\omega,T_1)-n(\omega',T_2))\Big\{\frac{1}{|\Delta|^2}e^{-2\,\mathrm{Im}(k_z)d}\\&((k_\rho^2-\beta k_0k_x)^2+\beta^2k_z^2k_y^2)\Big[(k_\rho^2-\beta k_0k_x)(1-|r_{1p}|^2)(1-|r_{2p}^{'}|^2)|D_{ss}|^2\\&+\beta^2k_z^2k_y^2(1-|r_{1p}|^2)(1-|r_{2s}^{'}|^2)|D_{sp}|^2+(p\to s)\Big]\Big\},\ \text{PWs}\\&N(\omega,k_x,k_y) = (n(\omega,T_1)-n(\omega',T_2))\Big\{\frac{4}{|\Delta|^2}e^{-2\,\mathrm{Im}(k_z)d}\\&((k_\rho^2-\beta k_0k_x)^2+\beta^2k_z^2k_y^2)\Big[(k_\rho^2-\beta k_0k_x)^2\,\mathrm{Im}(r_{1p})\,\mathrm{Im}(r_{2p}^{'})|D_{ss}|^2\\&-\beta^2k_z^2k_y^2\,\mathrm{Im}(r_{1p})\,\mathrm{Im}(r_{2s}^{'})\,|D_{sp}|^2+(p\to s)\Big]\Big\},\ \text{EWs}\end{aligned}\tag{A.39}$$

Here $k_\rho = \sqrt{k_x^2+k_y^2}$, $\beta = V/c$, $\gamma = 1/\sqrt{1-\beta^2}$, $k_0 = \omega/c$, $k_x^{'} = \gamma(k_x-\beta k_0)$, $\omega' = \gamma(\omega - k_xV)$, $k_z = \sqrt{k_0^2-k_\rho^2}$, $D_{ss} = 1-e^{2ik_zd}r_{1s}r_{2s}^{'}$, $D_{pp} = 1-e^{2ik_zd}r_{1p}r_{2p}^{'}$, $D_{sp} = 1+e^{2ik_zd}r_{1s}r_{2p}^{'}$, $D_{ps} = 1+e^{2ik_zd}r_{1p}r_{2s}^{'}$, $\Delta = (k_\rho^2-\beta k_0k_x)^2D_{ss}D_{pp} + \beta^2k_z^2k_y^2D_{sp}D_{ps}$. The symbol $p\leftrightarrow s$ denotes the terms that can be gained by permuting the indexes p and s of preceding terms. $r_{1(s,p)}$ are the reflection coefficients from the stationary plate, $r_{2(s,p)}^{'}$ are the reflection coefficients in the co-moving frame. Δ is the denominator of the matrix $(1-S_2S_1e^{2ik_zd})^{-1}$.

In the case $T_1 = T_2 = 0$K, under which condition $n(\omega, T)$ vanishes for positive frequencies and equals -1 for negative frequencies. In the lab frame, we only consider positive frequency photons, so essentially no photon emitted from plate 1. However, for the moving plate 2, the photon emission can be nonzero for negative Doppler shifted waves $\omega' < 0$, under which condition only photons with $k_x > \omega/V$ can be transferred.

The dominant term in the multi-reflection factor $\Delta = (k_\rho^2 - \beta k_0 k_x)^2 D_{ss} D_{pp} + \beta^2 k_z^2 k_y^2 D_{sp} D_{ps}$ is the term related to (p) polarized reflection coefficients $D_{pp} = 1 - e^{2ik_z d} r_{1p} r'_{2p}$. From the photon exchange term for the case with polarization mixing, we define the normalized Δ_N rather than Δ in Eq. (A.39) as the multi-reflection factor,

$$\Delta_N = \frac{(k_\rho^2 - \beta k_0 k_x)^2 D_{ss} D_{pp} + \beta^2 k_z^2 k_y^2 D_{sp} D_{ps}}{(k_\rho^2 - \beta k_0 k_x)^2 + \beta^2 k_z^2 k_y^2}. \tag{A.40}$$

In the region which supports the singular resonance $\beta < 10^{-4}$, since $k_x > k_0/\beta$, one has $\beta^2 k_z^2 k_y^2 \ll (k_\rho^2 - \beta k_0 k_x)^2$ and $D_{ss} \approx 1$. Thus Δ_N is well approximated by D_{pp}. At the phase balance wavevector $k_x^{PB} = 2\omega/V$, $D_{pp}(k_x^{PB}) = 1 - |r_p(\omega)|^2 e^{-4\omega d/V}$, we can adjust the distance d to make it zero as long as $|r_p| > 1$. It is clear that D_{pp} has a local minimum at $(\omega_{SWR}, k_x^{PB}, k_y = 0)$ due to the surface wave resonance (SWR) of $|r_p(\omega)|$. That D_{pp} equals zero at this minimum leads to

$$d_0 = \frac{V}{2\omega_{SWR}} \ln |r_p(\omega_{SWR})| . \tag{A.41}$$

Note that we achieve an upper bound on the critical distance.

A.6 Singular Resonance: Polarization mixing and relativistic effects

In the main text, we have assumed a non-relativistic Lorentz transform and no polarization mixing. We then find the conventional multi-reflection factor $1 - r_1 r_2 e^{2ik_z d}$ is real at the phase balance wavevector, which can lead to singular resonance at the critical distance. Here we show that the singular resonance can exist in spite of relativistic effects and polarization mixing.

At the relativistic phase balance wavevector, $k_x = (1 + 1/\gamma)\omega/V$, $\omega' = -\omega$, $k'_x = k_x$ (Eq. (A.27) and (A.28)). The frequency is opposite and the wavevector is unchanged, consistent with the invariance of the four dimensional

momentum vector. Due to the reality of fields, the reflection coefficients in the co-moving frame at frequency $-\omega$ are the complex conjugates of corresponding reflection coefficients in the lab frame at frequency ω, $r'_{2(s,p)} = r^*_{1(s,p)}$. We now note the critical fact that at this specific phase balance wavevector $\mathrm{Im}(D_{ss}) = \mathrm{Im}(D_{pp}) = \mathrm{Im}(D_{sp}D_{ps}) = 0$. D_{ss}, D_{pp} are real and $D_{sp} = D^*_{ps}$, so that the multi-reflection factor (Δ) which includes polarization mixing and relativistic effects is real valued at the relativistic phase balance vector. We emphasize that this situation is exactly equivalent to the simple multi-reflection factor we considered in the earlier discussion. Furthermore, in the presence of surface waves there will always exist a critical distance when this multi-reflection factor $\Delta = 0$. The main contribution in this work is this delicate phase balance and amplitude balance condition that has not been pointed out before.

A.7 Non-equilibrium vacuum friction

The dispersive force, i.e., the momentum transfer between the two plates [38], is the product of the total number of exchanged photons and the momentum of a single photon $\hbar k_x$($\hbar$ is the Planck constant divided by 2π)

$$f_x(\omega, k_x, k_y) = \hbar k_x N(\omega, k_x, k_y). \tag{A.42}$$

We also note that the energy transfer between the two plates is the product of the total number of photons exchanged and the energy of a single photon$\hbar\omega$.

The net dispersive force can be achieved by integrating all possible partial waves ω, $k_x$and k_y [38] in the above Eq. (A.42). Note that the frequency ω should be positive. The friction can be calculated by

$$F_x = \int_0^\infty \frac{d\omega}{2\pi} \int_{-\infty}^\infty \frac{dk_x}{2\pi} \int_{-\infty}^\infty \frac{dk_y}{2\pi} \hbar k_x N(\omega, k_x, k_y). \tag{A.43}$$

Note that Nhas different expressions for propagating and evanescent waves (see Eq. (A.39)). We can then recover the results in Ref. [96] which has a detailed calculation based on the stress tensor.

In the main text, we use the general theory here to generate the figures. At a fixed velocity 10^4m/s, the critical distance is found to be 10.04nm by Eq. (A.41). In Fig. 3.3 of the main text, k_y in Eq. (A.39) is integrated from $-\infty$ to ∞. Here we show the 3D plots of Fig. 3.3 to illustrate the peak due to

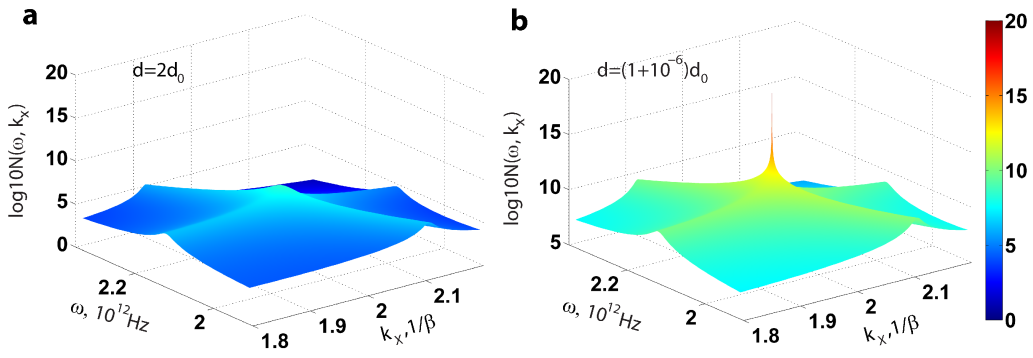

Figure A.1: (a) and (b) are the three dimensional version of Fig. 3.3(a) and (b) in the main text, respectively. The large peak in (b) due to the singular resonance is evident. Even though the resonance condition occurs at a single isolated point in reciprocal space, it leads to divergences in physical observables.

singular resonance more clearly.

In Fig. 3.3 of the main text, we have not integrated all the possible (ω, k_x, k_y) region in Eq. (A.43), but a small neighborhood around the singularity (ω_{SWR}, k_x^{PB}, $k_y = 0$), ω from $(1-0.05)\omega_{SWR}$ to $(1+0.05)\omega_{SWR}$, k_x from $(1-0.05)k_x^{PB}$ to $(1+0.05)k_x^{PB}$, and k_y from $-0.05k_x^{PB}$ to $+0.05k_x^{PB}$. In Fig. 3.4(b), the magnitudes of friction at $d_1 = 2d_0$ and $d_2 = (1+10^{-6})d_0$ are $4.58 \times 10^{-5}\mathrm{N/m^2}$ and $10.7\mathrm{N/m^2}$, respectively.

A.8 The scaling law of non-equilibrium vacuum friction

We have shown that at the phase balance wavevector, the denominator Δ_N of the integral Eq. (A.43) can be exactly zero. Thus we have a three dimensional improper integral. We emphasize that this resonance condition leads to a divergence in vacuum friction. Here, we rigorously prove the existence of this divergence and find the scaling law governing the vacuum friction near the resonance condition. The analytical scaling law is in excellent agreement with the numerical calculations.

At a given velocity V, we first fix k_x to be the phase balance wavevector so that Δ is real. At any distance$d$, we can find the minimum of Δ_N as a function of ω and k_y at (ω^0, k_y^0). We define d_0 as the critical distance so that the minimum at d_0 is zero. The minimum generally occurs at $k_y = 0$ and

ω_{SWR}, but our derivation below does not depend on this statement of the location of the minimum. At the critical distance d_0, we have a singular point $(\omega^0, k_x^{PB}, k_y^0)$ in three dimensional spaces (ω, k_x, k_y) where the denominator Δ_N is exact zero.

First we analyze the behavior of the denominator at this singular point. At the phase balance wavevector, Δ_N is real valued as a function of ω and k_y. As the function reaches the minimum, the first order derivatives of ω and k_y are zero. However, the first order derivative of k_x is not zero but a complex number since Δ is generally complex when k_x departs from k_x^{PB}. Therefore Δ_N can be approximated by $a_1\omega^2 + a_2k_y^2 + a_3k_x$ around the minimum. Here ω should be understood by $\omega - \omega_0$, the difference to the singularity, so are k_y and k_x. a_1 and a_2 are positive numbers, $a_3 = a_4 + ia_5$ is a complex number, the possible cross term ωk_y is not important here since we are looking for an upper bound of Δ_N. The denominator $|\Delta_N|^2$ will be approximated by $(a_1\omega^2 + a_2k_y^2 + a_4k_x)^2 + (a_5k_x)^2$. In a neighborhood of the minimum, we have

$$\frac{1}{2}((a_1\omega^2+a_2k_y^2+a_4k_x)^2+(a_5k_x)^2) < |\Delta_N|^2 < 2((a_1\omega^2+a_2k_y^2+a_4k_x)^2+(a_5k_x)^2) \tag{A.44}$$

The sign of a_4 here should be dealt with carefully. Firstly we consider the branch of k_x where a_4k_x is positive. If $a_4 > 0$, we choose the branch $k_x > 0$; if $a_4 < 0$ we choose the branch $k_x < 0$. Then we have

$$\left(a_1\omega^2 + a_2k_y^2\right)^2+(a_4k_x)^2 \leq (a_1\omega^2+a_2k_y^2+a_4k_x)^2 \leq 2\left(a_1\omega^2 + a_2k_y^2\right)^2+2(a_4k_x)^2 \tag{A.45}$$

For the asymptotic behavior, the constants a_i are not important. It is clear that there exists positive constants q and p so that,

$$q\left[(\omega^2 + k_y^2)^2 + k_x^2\right] < |\Delta_N|^2 < p\left[(\omega^2 + k_y^2)^2 + k_x^2\right]. \tag{A.46}$$

In the integral

$$\int d\omega dk_x dk_y \frac{1}{(\omega^2 + k_y^2)^2 + k_x^2}, \tag{A.47}$$

we first take $\omega = r\cos\theta, k_y = r\sin\theta$, so that the integral transforms to

$$\int dr^2 dk_x \frac{1}{(r^2)^2 + k_x^2} = \int dr dk_x \frac{1}{r^2 + k_x^2}. \tag{A.48}$$

Further by taking $r = \rho\cos\theta, k_x = \rho\sin\theta$, the integral will be

$$\int d\rho \frac{1}{\rho} \tag{A.49}$$

which diverges. Note that in the branch $a_4 k_x < 0$, the upper bound of $|\Delta_N|^2$ in Eq. (A.46) still satisfies; therefore the integral diverges in this branch also.

The scaling law can be seen just by an additional $d - d_0$ term $a_6 d$ (a_6 is positive) in the first order Taylor expansion of Δ_N. In a neighborhood of the minimum,

$$|\Delta_N|^2 \sim (a_1\omega^2 + a_2 k_y^2 + a_4 k_x + a_6 d)^2 + (a_5 k_x)^2 \,. \tag{A.50}$$

Following the same integration procedure, the integral will be

$$\int_0^\delta d\rho \frac{1}{\rho + d^2}, \tag{A.51}$$

where δ is a constant that Eq. (A.50) holds in the δ-neighborhood. This integral gives

$$\ln\frac{1}{d} + \text{constant}. \tag{A.52}$$

Thus the scaling law will be

$$F(d) \propto \ln(\frac{d_0}{d - d_0}), \tag{A.53}$$

where we have replaced d by $d - d_0$ and normalize it to d_0. It diverges very slowly as d approaches d_0.

A.9 The non-equilibrium vacuum friction varying with velocity

The phase balance condition for the resonance is achieved by the coupling of positive and negative frequencies whereas the amplitude balance condition is adjusted by tuning the distance between the mirrors while keeping the velocity of the moving mirror fixed. In this section we show that changing the velocity while keeping the distance constant also leads to the excitation of the resonance. We also derive the scaling law with respect to the velocity at a given

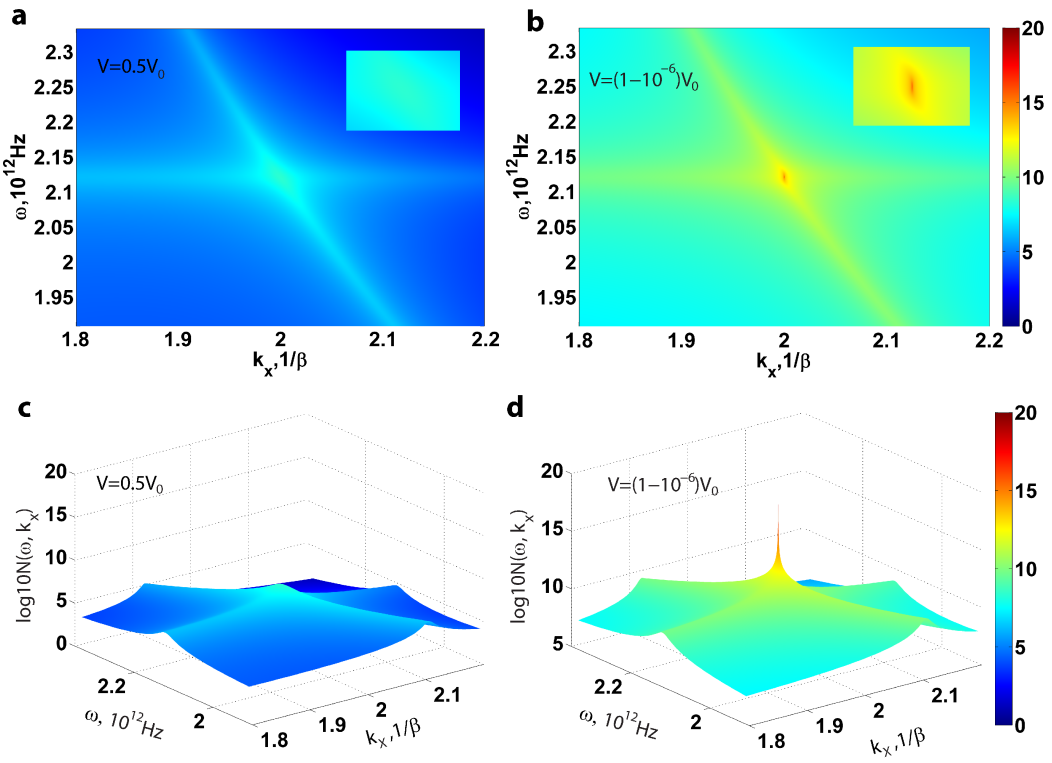

Figure A.2: Contribution to exchanged photon number (in log scale) resolved by frequency and lateral wavevector k_x (normalized to free space wavevector) at (a) $V = 0.5V_0$ and (b) $V \to V_0^-$. In both (a) and (b), we see two bright curves, both of which are due to surface wave resonances. The horizontal one comes from SWR at the interface of the stationary plate and vacuum while the other one is due to SWR at the interface of the moving plate and vacuum. These two bright curves join at the phase balance wavevector when the Doppler shifted SWR frequency in the co-moving frame is opposite to the SWR frequency in the lab frame. In (a), at a velocity much smaller than V_0, the singular resonance condition is far from being satisfied. However, the bright curves remain due to the SWR at the two interfaces. In (b), the red bright point is due to the singular resonance that arises since the amplitude balance condition is satisfied when $V \to V_0^-$ and $k_x = 2/\beta$. This leads to giant photon exchange between moving plates at the phase and amplitude balance condition. The insets give the zoom in plots near the intersection of the two SWRs. We emphasize the dramatic increase in the photon exchange due to the singular FP resonance of evanescent waves. (c) and (d) are the three dimensional version of (a) and (b), respectively. The large peak in (d) due to the singular resonance is evident.

distance using a similar approach.

To prove the divergence of friction and scaling law, we first fix the wavevector k_x to be the phase balance wavevector k_x^{PB}. The only difference is that k_x^{PB} is a function of the velocity, so that it is also a variable compared to the given velocity case where k_x^{PB}(normalized to free space wavevector) is a constant. However, this fact will not affect the second step, finding the velocity where the minimum of the multi-reflection factor Δ_N is exactly zero.

At all practical velocities, Δ_N at the phase balance wavevector is well approximated by $D_{pp}(k_x^{PB}) = 1 - |r_p(\omega)|^2 e^{-4\omega d/V}$ with $k_x^{PB} = 2\omega/V$. The minimum of $D_{pp}(k_x^{PB})$ occurs at $k_y = 0$ and ω_{SWR} where $|r_p(\omega)|$ has a resonance. That the minimum of $D_{pp}(k_x^{PB})$ equals zero gives the critical velocity V_0,

$$V_0 = d\frac{2\omega_{SWR}}{\ln|r_p(\omega_{SWR})|}. \tag{A.54}$$

Note that this equation is essentially the same to Eq. (A.41). These two equations suggest that d/V should be a constant at the singular resonance. Certainly, the velocity given by Eq. (A.54) should be practical.

The scaling law of friction to the velocity approaching the critical velocity will be

$$F(V) \propto \ln(\frac{V_0}{V_0 - V}). \tag{A.55}$$

which can be easily read from the derivation of Eq. (A.53). One can just replace d $(d - d_0)$ in Eq. (A.53) by $V(V_0 - V)$.

Here we present the results when the vacuum gap is fixed at 10nm, and compare the photon exchange and vacuum friction at different velocities. At this distance, the critical velocity V_0 where the multi-reflection factor Δ_N reaches zero is about 0.996×10^4m/s. Due to the same mathematical structure and similar parameters, the results here look close to that of fixed velocity case.

In Fig. A.2, we plot the spectrum of photons exchanged according to their frequency and wavevector in the lab frame. For a velocity V_1 which is away from the singular Fabry-Perot resonance condition of evanescent waves, we see two distinct bright regions in $\omega - k$ space through which photons are spontaneously exchanged between the two plates. The horizontal region corresponds to the surface wave resonance frequency of the stationary plate where all wavevectors are excited like in a conventional SWR. The curved region corresponds to the SWR frequency of the moving plate however the frequency is Doppler shifted and the region is curved instead of a straight line.

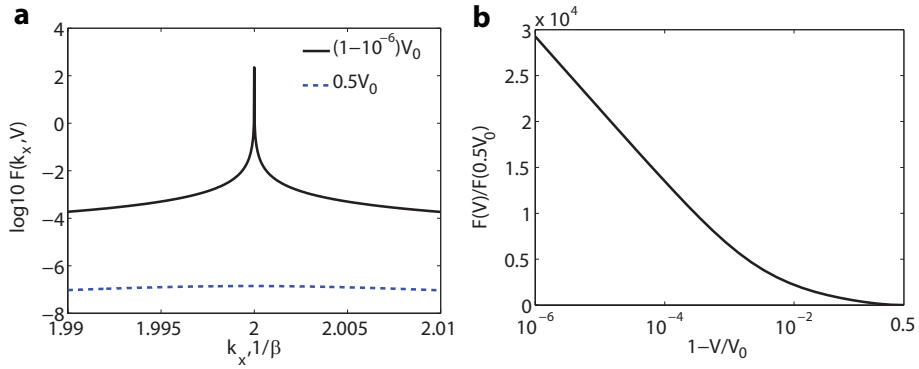

Figure A.3: Non-equilibrium vacuum friction on the FP plates (a) resolved by the wavevector k_x at $V = V_0^-$ and $V = 0.5V_0$. A major contribution to the force arises from modes at the perfect phase balance wavevector. However, at $0.5V_0$, the amplitude of friction is significantly smaller. (b) The distance dependence of friction at distances near V_0. The x axis is in $(1 - V/V_0)$ and log scale. We clearly see a linear increasing behavior as V approaches V_0. This is consistent with the theoretical scaling law which predicts a logarithmic divergence of the frictional force in the ideal limit.

In Fig. A.3(a), we plot the spectrum of the frictional force resolved according to the wavevector for various distances of the plates. The largest contribution to the force is due to the Fabry-Perot resonance of evanescent waves. When the velocity V approaches the critical distance V_0, the friction$F$scales as $\ln[V_0/(V_0 - V)]$. We plot the friction vs. velocity in Fig. A.3(b) to verify the theoretical predictions. The x axis is $(1 - V/V_0)$ and in log scale. We clearly see the friction increases linearly as a function of $\ln[V_0/(V_0 - V)]$ when V approaches V_0, consistent with the theoretical scaling law which predicts a divergence. Fig. A.3(b), the magnitudes of friction at $V_1 = 2V_0$ and $V_2 = (1 - 10^{-6})V_0$ are $3.70 \times 10^{-4}\mathrm{N/m^2}$ and $10.8\mathrm{N/m^2}$, respectively.

Bibliography

[1] SM Rytov, Yu. A Kravtsov, and VI Tatarskii. *Principles of statistical radiophysics. Vol. 3. Wave propagation through random media*. Springer, Berlin, 1989.

[2] LD Landau, EM Lifshitz, and LP Pitaevskii. *Statistical Physics, Part. 1*, volume 24. Pergamon Press, Oxford, 1980.

[3] W. Eckhardt. Macroscopic theory of electromagnetic fluctuations and stationary radiative heat transfer. *Phys. Rev. A*, 29(4):1991–2003, April 1984.

[4] Chen-To Tai. *Dyadic Green functions in electromagnetic theory*, volume 272. IEEE press New York, 1994.

[5] Jin Au Kong. *Electromagnetic wave theory*, volume 2. Wiley New York, 1990.

[6] EM Lifshitz. The theory of molecular attractive forces between solids. *Soviet Phys. JETP*, 2:73–83, 1956.

[7] D. Polder and M. Van Hove. Theory of radiative heat transfer between closely spaced bodies. *Phys. Rev. B*, 4(10):3303–3314, November 1971.

[8] Zhuomin Zhang. *Nano/Microscale Heat Transfer*. McGraw-Hill Professional, 2007.

[9] Gang Chen. *Nanoscale energy transport and conversion: a parallel treatment of electrons, molecules, phonons, and photons*. Oxford University Press, USA, 2005.

[10] S.-A. Biehs, P. Ben-Abdallah, F. S. S. Rosa, K. Joulain, and J.-J. Greffet. Nanoscale heat flux between nanoporous materials. *Opt. Express*, 19(S5):A1088–A1103, September 2011.

[11] Andrei V. Shchegrov, Karl Joulain, Rémi Carminati, and Jean-Jacques Greffet. Near-field spectral effects due to electromagnetic surface excitations. *Phys. Rev. Lett.*, 85(7):1548–1551, August 2000.

[12] Yu Guo, Cristian L. Cortes, Sean Molesky, and Zubin Jacob. Broadband super-planckian thermal emission from hyperbolic metamaterials. *Applied Physics Letters*, 101(13):131106–131106–5, September 2012.

[13] Karl Joulain, Jean-Philippe Mulet, François Marquier, Rémi Carminati, and Jean-Jacques Greffet. Surface electromagnetic waves thermally excited: Radiative heat transfer, coherence properties and casimir forces revisited in the near field. *Surface Science Reports*, 57(3–4):59–112, May 2005.

[14] M. Laroche, R. Carminati, and J.-J. Greffet. Near-field thermophotovoltaic energy conversion. *Journal of Applied Physics*, 100(6):063704–063704–10, September 2006.

[15] J. Lussange, R. Guérout, F. S. S. Rosa, J.-J. Greffet, A. Lambrecht, and S. Reynaud. Radiative heat transfer between two dielectric nanogratings in the scattering approach. *Phys. Rev. B*, 86(8):085432, August 2012.

[16] Igor S. Nefedov and Constantin R. Simovski. Giant radiation heat transfer through micron gaps. *Phys. Rev. B*, 84(19):195459, November 2011.

[17] Jean-Philippe Mulet, Karl Joulain, Rémi Carminati, and Jean-Jacques Greffet. Enhanced radiative heat transfer at nanometric distances. *Microscale Thermophysical Engineering*, 6(3):209–222, 2002.

[18] Arvind Narayanaswamy and Gang Chen. Thermal emission control with one-dimensional metallodielectric photonic crystals. *Phys. Rev. B*, 70(12):125101, September 2004.

[19] Emmanuel Rousseau, Alessandro Siria, Guillaume Jourdan, Sebastian Volz, Fabio Comin, Joël Chevrier, and Jean-Jacques Greffet. Radiative heat transfer at the nanoscale. *Nat Photon*, 3(9):514–517, September 2009.

[20] A. I. Volokitin and B. N. J. Persson. Radiative heat transfer between nanostructures. *Phys. Rev. B*, 63(20):205404, April 2001.

[21] A. I. Volokitin and B. N. J. Persson. Near-field radiative heat transfer and noncontact friction. *Rev. Mod. Phys.*, 79(4):1291–1329, October 2007.

[22] J. B. Pendry. Radiative exchange of heat between nanostructures. *J. Phys.: Condens. Matter*, 11(35):6621, September 1999.

[23] Karl Joulain, Jérémie Drevillon, and Philippe Ben-Abdallah. Noncontact heat transfer between two metamaterials. *Phys. Rev. B*, 81(16):165119, April 2010.

[24] Evgeny A. Vinogradov and Illarion A. Dorofeev. Thermally stimulated electromagnetic fields of solids. *Phys.-Usp.*, 52(5):425, May 2009.

[25] C. J. Fu and Z. M. Zhang. Nanoscale radiation heat transfer for silicon at different doping levels. *International Journal of Heat and Mass Transfer*, 49(9–10):1703–1718, May 2006.

[26] Clayton R. Otey, Wah Tung Lau, and Shanhui Fan. Thermal rectification through vacuum. *Phys. Rev. Lett.*, 104(15):154301, April 2010.

[27] Mathieu Francoeur, M. Pinar Mengüç, and Rodolphe Vaillon. Near-field radiative heat transfer enhancement via surface phonon polaritons coupling in thin films. *Applied Physics Letters*, 93(4):043109, July 2008.

[28] Lu Hu, Arvind Narayanaswamy, Xiaoyuan Chen, and Gang Chen. Near-field thermal radiation between two closely spaced glass plates exceeding planck's blackbody radiation law. *Applied Physics Letters*, 92(13):133106–133106–3, April 2008.

[29] Sheng Shen, Arvind Narayanaswamy, and Gang Chen. Surface phonon polaritons mediated energy transfer between nanoscale gaps. *Nano Lett.*, 9(8):2909–2913, August 2009.

[30] Xianliang Liu, Talmage Tyler, Tatiana Starr, Anthony F. Starr, Nan Marie Jokerst, and Willie J. Padilla. Taming the blackbody with infrared metamaterials as selective thermal emitters. *Phys. Rev. Lett.*, 107(4):045901, July 2011.

[31] Biswajeet Guha, Clayton Otey, Carl B. Poitras, Shanhui Fan, and Michal Lipson. Near-field radiative cooling of nanostructures. *Nano Lett.*, 12(9):4546–4550, September 2012.

[32] Yannick De Wilde, Florian Formanek, Rémi Carminati, Boris Gralak, Paul-Arthur Lemoine, Karl Joulain, Jean-Philippe Mulet, Yong Chen, and Jean-Jacques Greffet. Thermal radiation scanning tunnelling microscopy. *Nature*, 444(7120):740–743, December 2006.

[33] Arvind Narayanaswamy and Gang Chen. Surface modes for near field thermophotovoltaics. *Applied Physics Letters*, 82(20):3544–3546, May 2003.

[34] Andrew C. Jones and Markus B. Raschke. Thermal infrared near-field spectroscopy. *Nano Lett.*, 12(3):1475–1481, March 2012.

[35] Giuseppe Bimonte. Scattering approach to casimir forces and radiative heat transfer for nanostructured surfaces out of thermal equilibrium. *Phys. Rev. A*, 80(4):042102, October 2009.

[36] Matthias Krüger, Thorsten Emig, and Mehran Kardar. Nonequilibrium electromagnetic fluctuations: Heat transfer and interactions. *Phys. Rev. Lett.*, 106(21):210404, May 2011.

[37] Matthias Krüger, Giuseppe Bimonte, Thorsten Emig, and Mehran Kardar. Trace formulas for nonequilibrium casimir interactions, heat radiation, and heat transfer for arbitrary objects. *Phys. Rev. B*, 86(11):115423, September 2012.

[38] Mohammad F. Maghrebi, Ramin Golestanian, and Mehran Kardar. Scattering approach to the dynamical casimir effect. *Phys. Rev. D*, 87(2):025016, January 2013.

[39] R. Messina and M. Antezza. Casimir-lifshitz force out of thermal equilibrium and heat transfer between arbitrary bodies. *EPL*, 95(6):61002, September 2011.

[40] Riccardo Messina and Mauro Antezza. Scattering-matrix approach to casimir-lifshitz force and heat transfer out of thermal equilibrium between arbitrary bodies. *Phys. Rev. A*, 84(4):042102, October 2011.

[41] Sahand Jamal Rahi, Thorsten Emig, Noah Graham, Robert L. Jaffe, and Mehran Kardar. Scattering theory approach to electrodynamic casimir forces. *Phys. Rev. D*, 80(8):085021, October 2009.

[42] Mauro Antezza, Lev P. Pitaevskii, Sandro Stringari, and Vitaly B. Svetovoy. Casimir-lifshitz force out of thermal equilibrium and asymptotic nonadditivity. *Phys. Rev. Lett.*, 97(22):223203, November 2006.

[43] Giuseppe Bimonte and Enrico Santamato. General theory of electromagnetic fluctuations near a homogeneous surface in terms of its reflection amplitudes. *Phys. Rev. A*, 76(1):013810, July 2007.

[44] Giuseppe Bimonte. A theory of electromagnetic fluctuations for metallic surfaces and van der waals interactions between metallic bodies. *Phys. Rev. Lett.*, 96(16):160401, April 2006.

[45] M.T.H. Reid, A.W. Rodriguez, and S.G. Johnson. Fluctuation-induced phenomena in nanoscale systems: Harnessing the power of noise. *Proceedings of the IEEE*, 101(2):531–545, 2013.

[46] Alejandro W. Rodriguez, M. T. Homer Reid, and Steven G. Johnson. Fluctuating-surface-current formulation of radiative heat transfer for arbitrary geometries. *Phys. Rev. B*, 86(22):220302, December 2012.

[47] Alejandro W. Rodriguez, M. T. H. Reid, and Steven G. Johnson. Fluctuating-surface-current formulation of radiative heat transfer: Theory and applications. *Phys. Rev. B*, 88(5):054305, August 2013.

[48] Nader Engheta and Richard W Ziolkowski. *Metamaterials: physics and engineering explorations*. Wiley. com, 2006.

[49] Vladimir M. Shalaev. Optical negative-index metamaterials. *Nat Photon*, 1(1):41–48, January 2007.

[50] D. R. Smith, J. B. Pendry, and M. C. K. Wiltshire. Metamaterials and negative refractive index. *Science*, 305(5685):788–792, August 2004.

[51] J. B. Pendry. Negative refraction makes a perfect lens. *Phys. Rev. Lett.*, 85(18):3966–3969, October 2000.

[52] Viktor G. Veselago. The electrodynamics of substances with simultaneously negative values of \epsilon and \mu. *Sov. Phys. Usp.*, 10(4):509, April 1968.

[53] E. Plum, J. Zhou, J. Dong, V. A. Fedotov, T. Koschny, C. M. Soukoulis, and N. I. Zheludev. Metamaterial with negative index due to chirality. *Phys. Rev. B*, 79(3):035407, January 2009.

[54] Bingnan Wang, Jiangfeng Zhou, Thomas Koschny, Maria Kafesaki, and Costas M. Soukoulis. Chiral metamaterials: simulations and experiments. *J. Opt. A: Pure Appl. Opt.*, 11(11):114003, November 2009.

[55] Shuang Zhang, Yong-Shik Park, Jensen Li, Xinchao Lu, Weili Zhang, and Xiang Zhang. Negative refractive index in chiral metamaterials. *Phys. Rev. Lett.*, 102(2):023901, January 2009.

[56] Wenshan Cai, Uday K. Chettiar, Alexander V. Kildishev, and Vladimir M. Shalaev. Optical cloaking with metamaterials. *Nat Photon*, 1(4):224–227, April 2007.

[57] J. B. Pendry, D. Schurig, and D. R. Smith. Controlling electromagnetic fields. *Science*, 312(5781):1780–1782, June 2006.

[58] D. Schurig, J. J. Mock, B. J. Justice, S. A. Cummer, J. B. Pendry, A. F. Starr, and D. R. Smith. Metamaterial electromagnetic cloak at microwave frequencies. *Science*, 314(5801):977–980, November 2006.

[59] Nicholas Fang, Hyesog Lee, Cheng Sun, and Xiang Zhang. Sub–diffraction-limited optical imaging with a silver superlens. *Science*, 308(5721):534–537, April 2005.

[60] Zubin Jacob, Leonid V. Alekseyev, and Evgenii Narimanov. Optical hyperlens: Far-field imaging beyond the diffraction limit. *Opt. Express*, 14(18):8247–8256, September 2006.

[61] C. L. Cortes, W. Newman, S. Molesky, and Z. Jacob. Quantum nanophotonics using hyperbolic metamaterials. *J. Opt.*, 14(6):063001, June 2012.

[62] Yu Guo, Ward Newman, Cristian L. Cortes, and Zubin Jacob. Applications of hyperbolic metamaterial substrates. *Advances in OptoElectronics*, 2012, December 2012.

[63] Harish N. S. Krishnamoorthy, Zubin Jacob, Evgenii Narimanov, Ilona Kretzschmar, and Vinod M. Menon. Topological transitions in metamaterials. *Science*, 336(6078):205–209, April 2012.

[64] D. R. Smith and D. Schurig. Electromagnetic wave propagation in media with indefinite permittivity and permeability tensors. *Phys. Rev. Lett.*, 90(7):077405, February 2003.

[65] David R. Smith, Pavel Kolinko, and David Schurig. Negative refraction in indefinite media. *J. Opt. Soc. Am. B*, 21(5):1032–1043, May 2004.

[66] Viktor A. Podolskiy and Evgenii E. Narimanov. Strongly anisotropic waveguide as a nonmagnetic left-handed system. *Phys. Rev. B*, 71(20):201101, May 2005.

[67] S.-A. Biehs, M. Tschikin, and P. Ben-Abdallah. Hyperbolic metamaterials as an analog of a blackbody in the near field. *Phys. Rev. Lett.*, 109(10):104301, September 2012.

[68] Yu Guo and Zubin Jacob. Thermal hyperbolic metamaterials. *Opt. Express*, 21(12):15014–15019, June 2013.

[69] Constantin Simovski, Stanislav Maslovski, Igor Nefedov, and Sergei Tretyakov. Optimization of radiative heat transfer in hyperbolic metamaterials for thermophotovoltaic applications. *Opt. Express*, 21(12):14988–15013, June 2013.

[70] S.-A. Biehs, M. Tschikin, R. Messina, and P. Ben-Abdallah. Super-planckian near-field thermal emission with phonon-polaritonic hyperbolic metamaterials. *Applied Physics Letters*, 102(13):131106, April 2013.

[71] Yu Guo and Zubin Jacob. Fluctuational electrodynamics of hyperbolic metamaterials. *Journal of Applied Physics*, 115(23):234306, June 2014.

[72] Zubin Jacob, Igor I. Smolyaninov, and Evgenii E. Narimanov. Broadband purcell effect: Radiative decay engineering with metamaterials. *Applied Physics Letters*, 100(18):181105, April 2012.

[73] Anthony J. Hoffman, Leonid Alekseyev, Scott S. Howard, Kale J. Franz, Dan Wasserman, Viktor A. Podolskiy, Evgenii E. Narimanov, Deborah L. Sivco, and Claire Gmachl. Negative refraction in semiconductor metamaterials. *Nat Mater*, 6(12):946–950, December 2007.

[74] M. A. Noginov, Yu A. Barnakov, G. Zhu, T. Tumkur, H. Li, and E. E. Narimanov. Bulk photonic metamaterial with hyperbolic dispersion. *Applied Physics Letters*, 94(15):151105, April 2009.

[75] Pavel A. Belov, Constantin R. Simovski, and Pekka Ikonen. Canalization of subwavelength images by electromagnetic crystals. *Phys. Rev. B*, 71(19):193105, May 2005.

[76] W. Dickson, G. A. Wurtz, P. Evans, D. O'Connor, R. Atkinson, R. Pollard, and A. V. Zayats. Dielectric-loaded plasmonic nanoantenna arrays: A metamaterial with tuneable optical properties. *Phys. Rev. B*, 76(11):115411, September 2007.

[77] Jie Yao, Zhaowei Liu, Yongmin Liu, Yuan Wang, Cheng Sun, Guy Bartal, Angelica M. Stacy, and Xiang Zhang. Optical negative refraction in bulk metamaterials of nanowires. *Science*, 321(5891):930–930, August 2008.

[78] W. Eckhardt. First and second fluctuation-dissipation-theorem in electromagnetic fluctuation theory. *Optics Communications*, 41(5):305–309, May 1982.

[79] Omar Kidwai, Sergei V. Zhukovsky, and J. E. Sipe. Effective-medium approach to planar multilayer hyperbolic metamaterials: Strengths and limitations. *Phys. Rev. A*, 85(5):053842, May 2012.

[80] Dmitriy Korobkin, Burton Neuner III, Chris Fietz, Nikoletta Jegenyes, Gabriel Ferro, and Gennady Shvets. Measurements of the negative refractive index of sub-diffraction waves propagating in an indefinite permittivity medium. *Opt. Express*, 18(22):22734–22746, October 2010.

[81] Sean Molesky, Christopher J. Dewalt, and Zubin Jacob. High temperature epsilon-near-zero and epsilon-near-pole metamaterial emitters for thermophotovoltaics. *Opt. Express*, 21(S1):A96–A110, January 2013.

[82] Maria Tschikin, Svend-Age Biehs, Riccardo Messina, and Philippe Ben-Abdallah. On the limits of the effective description of hyperbolic materials in the presence of surface waves. *J. Opt.*, 15(10):105101, October 2013.

[83] J. Kim, V. P. Drachev, Z. Jacob, G. V. Naik, A. Boltasseva, E. E. Narimanov, and V. M. Shalaev. Improving the radiative decay rate for dye molecules with hyperbolic metamaterials. *Opt. Express*, 20(7):8100–8116, March 2012.

[84] Rémi Carminati and Jean-Jacques Greffet. Near-field effects in spatial coherence of thermal sources. *Phys. Rev. Lett.*, 82(8):1660–1663, February 1999.

[85] C. Henkel, K. Joulain, R. Carminati, and J.-J. Greffet. Spatial coherence of thermal near fields. *Optics Communications*, 186(1–3):57–67, December 2000.

[86] K. Joulain and C. Henkel. The near field correlation spectrum of a metallic film. *Appl. Phys. B*, 93(1):151–158, October 2008.

[87] Wah Tung Lau, Jung-Tsung Shen, Georgios Veronis, and Shanhui Fan. Spatial coherence of the thermal electromagnetic field in the vicinity of a dielectric slab. *Phys. Rev. E*, 76(1):016601, July 2007.

[88] Stefan Scheel and Stefan Buhmann. Macroscopic quantum electrodynamics - concepts and applications. *Acta Physica Slovaca. Reviews and Tutorials*, 58(5):675–809, October 2008.

[89] J. B. Pendry. Shearing the vacuum - quantum friction. *J. Phys.: Condens. Matter*, 9(47):10301, November 1997.

[90] E. V. Teodorovich. On the contribution of macroscopic van der waals interactions to frictional force. *Proc. R. Soc. Lond. A*, 362(1708):71–77, June 1978.

[91] L. S. Levitov. Van der waals' friction. *EPL*, 8(6):499, March 1989.

[92] G. Barton. The quantum radiation from mirrors moving sideways. *Annals of Physics*, 245(2):361–388, February 1996.

[93] J. B. Pendry. Can sheared surfaces emit light? *Journal of Modern Optics*, 45(11):2389–2408, 1998.

[94] A. I. Volokitin and B. N. J. Persson. Theory of friction: the contribution from a fluctuating electromagnetic field. *J. Phys.: Condens. Matter*, 11(2):345, January 1999.

[95] A.A. Kyasov and G.V. Dedkov. Relativistic theory of fluctuating electromagnetic slowing down of neutral spherical particles moving in close vicinity to a flat surface. *Nuclear Instruments and Methods in Physics Research Section B: Beam Interactions with Materials and Atoms*, 195(3–4):247–258, October 2002.

[96] A. I. Volokitin and B. N. J. Persson. Theory of the interaction forces and the radiative heat transfer between moving bodies. *Phys. Rev. B*, 78(15):155437, October 2008.

[97] Stefan Scheel and Stefan Yoshi Buhmann. Casimir-polder forces on moving atoms. *Phys. Rev. A*, 80(4):042902, October 2009.

[98] T. G. Philbin and U. Leonhardt. No quantum friction between uniformly moving plates. *New J. Phys.*, 11(3):033035, March 2009.

[99] Gabriel Barton. On van der waals friction. II: Between atom and half-space. *New J. Phys.*, 12(11):113045, November 2010.

[100] G. V. Dedkov and A. A. Kyasov. Dynamical van der waals atom–surface interaction. *Surface Science*, 605(11–12):1077–1081, June 2011.

[101] Johan S. Høye and Iver Brevik. Casimir friction between dense polarizable media. *Entropy*, 15(8):3045–3064, July 2013.

[102] Gregor Pieplow and Carsten Henkel. Fully covariant radiation force on a polarizable particle. *New J. Phys.*, 15(2):023027, February 2013.

[103] Lukas Novotny and Bert Hecht. *Principles of nano-optics*. Cambridge university press, 2006.

[104] S.-A. Biehs, E. Rousseau, and J.-J. Greffet. Mesoscopic description of radiative heat transfer at the nanoscale. *Phys. Rev. Lett.*, 105(23):234301, December 2010.

[105] Z. Jacob, J.-Y. Kim, G. V. Naik, A. Boltasseva, E. E. Narimanov, and V. M. Shalaev. Engineering photonic density of states using metamaterials. *Appl. Phys. B*, 100(1):215–218, July 2010.

[106] Owen D. Miller, Steven G. Johnson, and Alejandro W. Rodriguez. The effectiveness of thin films in lieu of hyperbolic metamaterials in the near field. *arXiv:1311.5812 [physics]*, November 2013.

[107] L.D. Landau, E.M. Lifshitz, and L.P. Pitaevskij. *Statistical Physics: Part 2 : Theory of Condensed State*. Landau and Lifshitz Course of theoretical physics. Oxford, 1980.

[108] Karl Joulain, Rémi Carminati, Jean-Philippe Mulet, and Jean-Jacques Greffet. Definition and measurement of the local density of electromagnetic states close to an interface. *Phys. Rev. B*, 68(24):245405, December 2003.

[109] Vladyslav A. Golyk, Matthias Krüger, and Mehran Kardar. Heat radiation from long cylindrical objects. *Phys. Rev. E*, 85(4):046603, April 2012.

[110] Alexander P. McCauley, M. T. Homer Reid, Matthias Krüger, and Steven G. Johnson. Modeling near-field radiative heat transfer from sharp objects using a general three-dimensional numerical scattering technique. *Phys. Rev. B*, 85(16):165104, April 2012.

[111] Clayton R. Otey, Linxiao Zhu, Sunil Sandhu, and Shanhui Fan. Fluctuational electrodynamics calculations of near-field heat transfer in non-planar geometries: A brief overview. *Journal of Quantitative Spectroscopy and Radiative Transfer*, 132:3–11, January 2014.

[112] Gerald T. Moore. Quantum theory of the electromagnetic field in a variable-length one-dimensional cavity. *Journal of Mathematical Physics*, 11(9):2679–2691, September 1970.

[113] V. V. Dodonov. Current status of the dynamical casimir effect. *Phys. Scr.*, 82(3):038105, September 2010.

[114] C. M. Wilson, G. Johansson, A. Pourkabirian, M. Simoen, J. R. Johansson, T. Duty, F. Nori, and P. Delsing. Observation of the dynamical casimir effect in a superconducting circuit. *Nature*, 479(7373):376–379, November 2011.

[115] M Wolf and E Born. *Principles of optics: electromagnetic theory of propagation, interference and diffraction of light*. Cambridge University Press, 1980.

[116] LD Landau, EM Lifshitz, and LP Pitaevskii. *Electrodynamics of continuous media*. Pergamon Press, Oxford, 1984.

[117] F. Intravaia and A. Lambrecht. Surface plasmon modes and the casimir energy. *Phys. Rev. Lett.*, 94(11):110404, March 2005.

[118] A. I. Volokitin and B. N. J. Persson. Comment on 'no quantum friction between uniformly moving plates'. *New J. Phys.*, 13(6):068001, June 2011.

[119] Mehran Kardar and Ramin Golestanian. The "friction" of vacuum, and other fluctuation-induced forces. *Rev. Mod. Phys.*, 71(4):1233–1245, July 1999.

[120] Jeffrey M. McMahon, Stephen K. Gray, and George C. Schatz. Nonlocal optical response of metal nanostructures with arbitrary shape. *Phys. Rev. Lett.*, 103(9):097403, August 2009.

[121] Søren Raza, Giuseppe Toscano, Antti-Pekka Jauho, Martijn Wubs, and N. Asger Mortensen. Unusual resonances in nanoplasmonic structures due to nonlocal response. *Phys. Rev. B*, 84(12):121412, September 2011.

[122] Frank H. L. Koppens, Darrick E. Chang, and F. Javier García de Abajo. Graphene plasmonics: A platform for strong light–matter interactions. *Nano Lett.*, 11(8):3370–3377, August 2011.

[123] Victor W. Brar, Min Seok Jang, Michelle Sherrott, Josue J. Lopez, and Harry A. Atwater. Highly confined tunable mid-infrared plasmonics in graphene nanoresonators. *Nano Lett.*, 13(6):2541–2547, June 2013.

[124] Rongkuo Zhao, Alejandro Manjavacas, F. Javier García de Abajo, and J. B. Pendry. Rotational quantum friction. *Phys. Rev. Lett.*, 109(12):123604, September 2012.

[125] A. I. Volokitin and B. N. J. Persson. Quantum friction. *Phys. Rev. Lett.*, 106(9):094502, March 2011.

[126] Y. D. Chong, Li Ge, Hui Cao, and A. D. Stone. Coherent perfect absorbers: Time-reversed lasers. *Phys. Rev. Lett.*, 105(5):053901, July 2010.

[127] T. G. Philbin and U. Leonhardt. Casimir-lifshitz force between moving plates at different temperatures. *arXiv:0904.2148 [quant-ph]*, April 2009.

[128] Thomas G. Philbin, Chris Kuklewicz, Scott Robertson, Stephen Hill, Friedrich König, and Ulf Leonhardt. Fiber-optical analog of the event horizon. *Science*, 319(5868):1367–1370, March 2008.

[129] T. J. Kippenberg and K. J. Vahala. Cavity optomechanics: Back-action at the mesoscale. *Science*, 321(5893):1172–1176, August 2008.

[130] Peter W Milonni. *The quantum vacuum: an introduction to quantum electrodynamics*. Academic Press, 1994.

[131] E. Rubino, J. McLenaghan, S. C. Kehr, F. Belgiorno, D. Townsend, S. Rohr, C. E. Kuklewicz, U. Leonhardt, F. König, and D. Faccio. Negative-frequency resonant radiation. *Phys. Rev. Lett.*, 108(25):253901, June 2012.

[132] C. Ciracì, R. T. Hill, J. J. Mock, Y. Urzhumov, A. I. Fernández-Domínguez, S. A. Maier, J. B. Pendry, A. Chilkoti, and D. R. Smith. Probing the ultimate limits of plasmonic enhancement. *Science*, 337(6098):1072–1074, August 2012.

[133] Ryogo Kubo. Statistical-mechanical theory of irreversible processes. i. general theory and simple applications to magnetic and conduction problems. *Journal of the Physical Society of Japan*, 12(6):570–586, 1957.

[134] Mohammad F. Maghrebi, Robert L. Jaffe, and Mehran Kardar. Spontaneous emission by rotating objects: A scattering approach. *Phys. Rev. Lett.*, 108(23):230403, June 2012.